Research Square

Preprints are preliminary reports that have not undergone peer review.
They should not be considered conclusive, used to inform clinical practice,
or referenced by the media as validated information.

Microglial Perilipin-2 Deficiency Ameliorates Ischemic White Matter Injury via Lipid Metabolic Reprogramming

yi xie
Huazhong University of Science and Technology
xinyue wang
Tsinghua University
shuai liu
Huazhong University of Science and Technology
ziyu he
Huazhong University of Science and Technology
hang zhang
Huazhong University of Science and Technology
zhiyuan yu
Huazhong University of Science and Technology
minjie xie
Huazhong University of Science and Technology
wei wang
wwang@vip.126.com

Huazhong University of Science and Technology

Research Article

Keywords: Chronic cerebral hypoperfusion, White matter lesions, Microglia, PLIN2, Lipid droplet

Posted Date: May 22nd, 2026

DOI: https://doi.org/10.21203/rs.3.rs-9688977/v1

License: This work is licensed under a Creative Commons Attribution 4.0 International License.
Read Full License

Additional Declarations: No competing interests reported.

Abstract

Background

Chronic cerebral hypoperfusion-induced white matter lesions are a major contributor to vascular cognitive impairment in aging, characterized by microglial activation and defective clearance of cholesterol-rich myelin debris. Perilipin-2 (PLIN2), a key lipid droplet (LD)-associated protein involved in myelin metabolism, has an undefined role in ischemic white matter injury.

Methods

Microglia-specific *Plin2* knockout (*Plin2*$^{-/-}$) mice were subjected to bilateral common carotid artery stenosis (BCAS) to model cerebral hypoperfusion. Cognitive function, white matter integrity, and microglial phenotype were assessed. In parallel, integrated microglial transcriptomic and lipidomic analyses were performed to characterize inflammatory states and lipid metabolic profiles. Furthermore, the autophagy inhibitor chloroquine (CQ) was used *in vivo* and *in vitro* to test mechanistic dependence on autophagy.

Results

Plin2 deletion rescued BCAS-induced cognitive and motor deficits, attenuated white matter damage, and promoted remyelination. *Plin2*$^{-/-}$ microglia exhibited enhanced clearance of myelin-derived LDs and a reduced pro-inflammatory state, driven by an upregulation of the autophagy-lysosomal pathway (lipophagy). Crucially, CQ treatment abolished these neuroprotective effects, as evidenced by re-induced LD accumulation, and reinstated inflammatory activation in *Plin2*$^{-/-}$ mice and cultured microglia.

Conclusion

Microglial *Plin2* deletion protects against hypoperfusion injury by enhancing LD clearance, reprogramming lipid metabolism, and suppressing neuroinflammation in an autophagy-dependent manner. Clinically, PLIN2 may represent a promising therapeutic target for ischemic white matter injury and vascular cognitive impairment.

1. Introduction

Vascular cognitive impairment (VCI) ranks among the most common causes of dementia, imposing a heavy disease burden. Its prevalence escalates with age, presenting a growing challenge for aging populations worldwide[1]. The principal pathological substrate of VCI is chronic white matter injury secondary to cerebral hypoperfusion, progressing through a cascade of hypoxia-related events. This

cascade involves blood-brain barrier impairment, activation of glial cells, and eventual focal demyelination[2]. Risk-factor control (e.g., hypertension, dyslipidemia) remains the mainstay of VCI management, yet with limited efficacy, emphasizing the urgent need for novel and effective pharmacological strategies[1, 3].

Neuroinflammation plays a central role in mediating white matter damage under chronic hypoperfusion[4]. The accumulation of cholesterol-rich myelin debris in demyelinated foci acts as a potent trigger, sustaining and amplifying neuroinflammation[5]. Within lesion areas, inflammatory processes impede the migration and maturation of oligodendrocyte precursor cells (OPCs), curtail their differentiation into myelinating oligodendrocytes, and ultimately obstruct remyelination and tissue repair, which are critical determinants of white matter pathology[6]. Thus, attenuating local inflammation is a pivotal therapeutic objective for mitigating the progression of white matter damage.

As the resident immune cells of the central nervous system (CNS), microglia are critical regulators of neuroinflammatory responses. Under physiological conditions, they phagocytose damaged or aged myelin, thereby restraining inflammation and maintaining cerebral homeostasis[7, 8]. However, excessive uptake of myelin debris leads to pronounced intracellular lipid droplets (LDs) formation. Impaired clearance of these LDs results in their persistent accumulation, propelling microglia toward a pro-inflammatory state that actively suppresses myelin repair[9, 10]. In line with this, trehalose, a natural disaccharide that stimulates microglial lipid degradation, has been shown to reduce cholesteryl ester accumulation, attenuate pro-inflammatory cytokine release, and promote remyelination as well as functional recovery in inflammatory demyelination models[11]. These findings collectively suggest that modulating microglial lipid metabolism may be a promising strategy to counter inflammation and foster repair in ischemic demyelinating conditions.

Perilipin-2 (PLIN2), a core member of the perilipin protein family, serves as the predominant coat protein on LD and functions to segregate the neutral lipid core from the aqueous cytosol, thereby maintaining LD stability and metabolic homeostasis[12]. PLIN2 participates in multiple facets of LD dynamics, including their formation, fusion, lipolysis, and autophagic turnover (lipophagy)[12]. Evidence from diverse disease settings underscores the functional importance of PLIN2. In a murine model of atherosclerosis, *Plin2* knockout inhibits foam cell formation and promotes lipid efflux, thereby significantly suppressing the progression of atherosclerotic plaques[13]. In the context of hepatic lipid metabolism, *Plin2* deficiency remarkably reduces hepatic triglyceride (TG) content by enhancing autophagy (i.e., lipophagy), effectively ameliorating hepatic steatosis[14]. Additionally, in myelin-focused intervention experiments, *Plin2* deficiency in macrophages upregulates the expression of lipolysis-related lipases, facilitates cholesterol efflux, and ultimately decreases the intracellular LD burden[9]. Based on these findings, we hypothesize that targeting PLIN2 to modulate microglial lipid metabolism may represent a potential therapeutic strategy for ischemic demyelinating disorders.

To address this gap, the present study investigated the effects of *Plin2* deficiency on cognitive deficits, demyelinating lesions, microglial lipid metabolism, and neuroinflammation in a mouse model of bilateral

common carotid artery stenosis (BCAS)-induced white matter injury. Furthermore, integrated multi-omics analyses (transcriptomic and metabolomic profiling) were employed to elucidate the mechanisms by which PLIN2 influences LD degradation and inflammatory responses in myelin debris-engulfed microglia. Through these approaches, we aimed to determine whether PLIN2 represents a promising therapeutic target for ischemic white matter injury and VCI in clinical practice.

2. Materials and methods

2.1 | Animals

The *Plin2* conditional knockout mouse lines used in this study were obtained from Cyagen Biosciences (Suzhou) Inc. Male mice heterozygous for the *Plin2*-floxed allele were crossed with CX3CR1-Cre transgenic mice to generate offspring with microglia-specific *Plin2* knockout. All mice, including their offspring, were housed under specific pathogen-free (SPF) conditions in a controlled environment (22°C, 12-hour light/dark cycle) with free access to food and water. All animal experiments were conducted in accordance with the ARRIVE guidelines[15]. All animal procedures were approved by the Institutional Animal Care and Use Committee of Tongji Hospital, Tongji Medical College, Huazhong University of Science and Technology (Permit Number: TJH-202304028). Animals were randomly assigned to different groups, and each animal was labeled with a unique identification number generated using software.

2.2 | Bilateral common carotid artery stenosis (BCAS) surgery

Chronic cerebral hypoperfusion was induced in 8- to 10-week-old littermate controls ($Plin2^{fl/fl}$) and microglial-specific *Plin2*-deficient mice ($Cx3cr1^{Cre/+}$; $Plin2^{fl/fl}$) using the BCAS model, as previously described[16]. Briefly, mice were anesthetized with isoflurane (3% for induction, 1.0-1.5% for maintenance). A midline cervical incision was made to expose the bilateral common carotid arteries, which were then carefully isolated. Micro-coils (internal diameter, 0.18 mm; Sawane Spring Co.) were then applied to both arteries to induce stenosis. Sham-control animals underwent the same surgical procedure, including vessel exposure, but without coil placement.

2.3 | Chloroquine (CQ) treatment

Following BCAS surgery, $Cx3cr1^{Cre/+}$; $Plin2^{fl/fl}$ mice were randomly assigned to treatment groups. They received daily intraperitoneal injections of either chloroquine (50 mg/kg) or an equivalent volume of the vehicle control (1% dimethyl sulfoxide) for one month. The chloroquine dosage and treatment duration were selected based on previous studies[17].

2.4 | Cerebral Blood Flow (CBF) Measurement

CBF was assessed using laser speckle flowmetry (Omegazone, Omegawave Inc., Tokyo, Japan). Under deep isoflurane anesthesia (1–2% delivered via face mask), a midline incision was made to expose the skull, which was then thinned and rendered transparent using an optical clearing agent to enhance

visualization of the underlying vasculature. CBF was monitored at two time points: pre-surgery (baseline) and immediately after bilateral carotid artery stenosis. Data were expressed as a percentage of the baseline value. For quantitative analysis, at least four regions of interest (ROIs) were analyzed per mouse.

2.5 | Morris Water Maze (MWM) Test

Spatial learning and memory were assessed using the MWM test as previously described[18]. The protocol consisted of a 5 5-day acquisition phase followed by a probe test on day 6. During the acquisition phase, mice underwent four trials per day from four different start points around the pool, with a maximum latency of 60 s to locate the submerged platform. The probe test was conducted 24 hours after the final training session by removing the platform. Memory retention was evaluated by measuring the time spent in the target quadrant (south-west) where the platform had been located.

2.6 | Novel Object Recognition (NOR) Test

The NOR test was conducted as previously described[19]. Briefly, 24 hours before testing, mice were acclimated to the empty open-field arena for 15 min. On the testing day, each mouse was first subjected to a 5-min familiarization phase with two identical objects placed in the arena. After a 1-hour interval, one of the familiar objects was replaced with a novel object, and the mouse was allowed to explore both for 5 min during the discrimination phase. The time spent on the new (N) and familiar (F) objects was recorded using ANY-maze software, and the discrimination index (DI) was calculated as (N-F)/(N + F).

2.7 | Open Field Test (OFT)

The OFT was conducted as previously described[20]. Briefly, each mouse was gently placed in the center of a square, open-field arena and allowed to explore freely for 5 min. The test session was recorded by a video camera positioned above the arena. The total distance travelled by the mouse was quantified to assess general locomotor activity. Additionally, the time spent by the mouse in the central zone of the arena was recorded to evaluate anxiety-like behavior. The arena was thoroughly cleaned with 70% ethanol between each test session to eliminate olfactory cues.

2.8 | TreadScan Gait Analysis

We evaluated motor performance with the TreadScan system[21]. Mice were first trained for 2 consecutive days (two 1-min sessions per day at 6 cm/s) to walk on a motorized treadmill, and then underwent a 20-s test session at the same speed. Gait was recorded from a ventral view using a high-speed camera and a mirror. The TreadScan software (Clever Sys) automatically quantified gait parameters, including stance duration, stride length, and track width, and other spatiotemporal gait variables. Subsequently, R software was employed to perform comprehensive bioinformatic analyses on the obtained data, including partial least squares discriminant analysis (PLS-DA) for group differentiation and clustering analysis for generating heatmaps to visualize the expression patterns of the parameters[22].

2.9 | Tissue preparation

After induction of deep anesthesia with 5% isoflurane, mice were transcardially perfused with 20 mL of pre-cooled PBS followed by 20 mL of 4% paraformaldehyde (PFA). Following decapitation, the brain was fixed at 4°C for 18 hours and then gradually dehydrated with 10%, 20%, and 30% sucrose solutions. Serial coronal sections with a thickness of 16 μm were cut using a constant temperature freezing microtome (Thermo cryoStar NX50) at -20°C. The sections were then stored at -80°C until further use.

2.10 | Fluorescence-Activated Cell Sorting (FACS)

Microglia were isolated using FACS on a Moflo XDP sorter (Beckman Coulter). Firstly, the corpus callosum was microdissected and dissociated into a single-cell suspension using the Adult Brain Dissociation Kit for mice and rats (Miltenyi, 130-107-677). Cells were first blocked with an Fc receptor antibody (BD Biosciences, 553141; 1:100) for 15 min. They were then stained with a cocktail of fluorescent antibodies—CD11b-FITC (BioLegend, 101205; 1:200), CD45-APC (BioLegend, 157606; 1:200), and Tmem119-PE-Cyanine7 (Invitrogen, 25-6119; 1:200)—for 30 min on ice in the dark. Prior to sorting, cell viability was assessed by staining with 7-AAD (BD Biosciences, 559925; 1:20) for 5 min at room temperature in the dark. Viable microglia (7-AAD$^-$ CD11b$^+$ CD45$^{+/-}$) were isolated as previously described[23].

2.11 | Bulk RNA-Sequencing

Microglia from the mouse corpus callosum were isolated by FACS. Total RNA was extracted from approximately 300 sorted cells (viability ~ 90%) and reverse-transcribed into double-stranded cDNA using the Smart-seq2 amplification protocol. After cDNA synthesis and quality control, qualified amplified cDNAs were used for further library construction and sequencing.

For bioinformatic analyses, differential gene expression between groups was assessed using the DESeq2 R package (v1.42.1). Genes with an adjusted p-value (Q value) < 0.05 and an absolute $\log_2$ fold change > 1 were defined as differentially expressed genes (DEGs). Gene Ontology (GO) and Kyoto Encyclopedia of Genes and Genomes (KEGG) pathway enrichment analyses were performed using the clusterProfiler R package (v4.0.5), with significance set at a p-value < 0.05. Additionally, Gene Set Enrichment Analysis (GSEA) was carried out using the GSEA software against the Molecular Signatures Database (MSigDB) collections, including canonical pathways from C2 (KEGG, Reactome) and biological processes from C5 (GO). The normalized enrichment score (NES) and false discovery rate (FDR) were used to identify significantly enriched pathways.

2.12 | Preparation and fluorescent labeling of myelin debris

Myelin was purified from the brains of wild-type C57BL/6 mice according to an established protocol[24]. In brief, brain tissue was homogenized in 0.32 M sucrose and layered over a cushion of 0.85 M sucrose. After ultracentrifugation (75,000 × g, 4°C, 30 min), the myelin-enriched interface was collected and subjected to two osmotic shocks with ddH_2O, followed by subsequent centrifugation steps. The purified myelin was then resuspended in PBS. For fluorescent tracking, the myelin was labeled with the lipophilic dye PKH26 (Sigma, MINI26) following the manufacturer's instructions.

2.13 | Primary Microglial Culture and Treatment

Primary microglia were isolated from postnatal day 0–3 (P0-P3) C57BL/6 mouse pups as previously described[25]. Mixed glial cultures were maintained in high-glucose DMEM supplemented with 20% fetal bovine serum (FBS) for 11–13 days. Microglia were then detached from the astrocytic monolayer by orbital shaking (200 rpm, 2 h, 37°C). The harvested microglia were seeded at densities of 8×10^5 cells per well in 6-well plates and 4×10^4 cells per well in 24-well plates, and allowed to adhere for 24 hours in high-glucose DMEM containing 10% FBS prior to experimentation.

For *in vitro* treatments, cells were exposed to myelin debris (50 μg/mL), lipopolysaccharide (LPS, 1 μg/mL; Sigma), or the autophagy inhibitor chloroquine (CQ, 20 μM; MedChemExpress). The concentrations and treatment durations were optimized based on previous literature and our preliminary data[21, 26].

2.14 | siRNA-mediated *Plin2* Knockdown in Cultured Microglia

Plin2 knockdown in cultured microglia was performed via siRNA transfection using Lipofectamine 3000 (Invitrogen, L3000015). On the day of transfection, si-*Plin2* or control siRNA (si-NC; final concentration ~ 50 nM) was complexed with Lipofectamine 3000 in Opti-MEM according to the manufacturer's protocol. After a 10–15 min incubation at room temperature to allow complex formation, the siRNA-lipofectamine complexes (250 μL per well) were added to cells after removal of the old medium and the plates were incubated at 37°C. PLIN2 protein levels were assessed by Western blot 48 h after transfection to verify knockdown efficiency.

2.15 | BODIPY Staining and Lipid Droplet Quantification *In Vitro*

Intracellular lipid droplets (LDs) were stained with BODIPY 493/503 (1:1000, Thermo Fisher, D3922) for 10 minutes at room temperature. Following three washes with PBS, the samples were processed for quantitative analysis. For morphological assessment, images were acquired using a laser scanning confocal microscope (Olympus FV500). The number of LDs per cell was quantified with ImageJ software by applying a combination of automated particle analysis (with thresholds set for size and circularity) and manual verification to ensure counting accuracy[27–29].

For flow cytometric analysis, the fluorescence intensity of BODIPY 493/503 was measured using the FITC channel on a NovoCyte 3000 flow cytometer (Agilent)[30], and data were analyzed with FlowJo software.

2.16 | Lipidomics of Microglia *In Vitro*

Cellular samples were snap-frozen in liquid nitrogen for lipidomic analysis. Lipids were extracted via a methyl tert-butyl ether (MTBE)-based method, and profiled on a Nexera UPLC system (Shimadzu)

coupled to a Q Exactive Plus mass spectrometer (Thermo Fisher Scientific) with a heated electrospray ionization (HESI) source. A pooled quality control (QC) sample (aliquots of all individual samples) was analyzed intermittently to monitor instrumental stability.

Raw data were processed using LipidSearch software (v4.1, Thermo Fisher Scientific) for lipid identification and quantification (precursor/product ion mass tolerance: 5 ppm; M-score threshold: 5.0; identification grades A-D accepted). Data matrices from positive and negative ionization modes were merged, and lipids with > 50% missing values in any experimental group were excluded from further analysis. The filtered dataset was then analyzed and visualized using R software, with results presented as a heatmap.

2.17 | Luxol Fast Blue (LFB) Staining

Myelin integrity in the white matter was assessed histologically using LFB staining, as previously described[31]. In brief, brain sections were incubated in preheated 0.1% LFB solution (Servicebio, G1030) at 60°C for 6–8 hours. After cooling to room temperature, sections were rinsed thoroughly with distilled water and differentiated in a 0.05% lithium carbonate solution, followed by a rinse in 75% ethanol. The sections were then dehydrated through a graded ethanol series (75%, 90%, and 100%), cleared, and mounted. Images were acquired using an optical microscope (BX51, Olympus, Japan). The severity of white matter lesions was evaluated in a blinded manner and graded on a scale of 0 to 3, as follows: 0 (normal), 1 (disorganized nerve fiber arrangement), 2 (marked cavitation), and 3 (extensive loss of myelin fibers)[32].

2.18 | Immunofluorescence (IF) Staining and Quantification

For IF staining, frozen tissue sections or 4% PFA-fixed cultured cells were permeabilized with 0.3% Triton X-100 in PBS for 15 minutes and then blocked with 10% bovine serum albumin for 1 hour at room temperature. Samples were incubated with primary antibodies overnight at 4°C, followed by three 10-minute washes in PBS. Subsequently, they were incubated with appropriate fluorescently conjugated secondary antibodies (Invitrogen) for 1 hour at room temperature in the dark. After final washes, the sections were mounted with an anti-fade mounting medium containing DAPI (Beyotime, P0131) to visualize nuclei.

Stained samples were imaged using either a fluorescence microscope (BX51, Olympus) or a laser scanning confocal microscope (FV500, Olympus). Quantitative analysis was performed by an investigator blinded to the experimental groups using ImageJ software (NIH, USA). The density of positive cells (cells/mm²), the mean fluorescence intensity, and the proportion of positive cells were quantified. Three-dimensional reconstruction of microglial morphology was performed using Imaris Viewer software (Bitplane). A list of all primary antibodies used is provided in **Table S1.**

2.19 | Electron Microscopy

At 30 days post-BCAS, mice were transcardially perfused with PBS under deep anesthesia. The corpus callosum was rapidly dissected and cut into ~ 1 mm³ pieces, which were then fixed in 2.5%

glutaraldehyde for 4 hours at room temperature and stored at 4°C until further processing. Ultrastructural imaging was performed using a Hitachi HT7700 electron microscope operated at 120 kV. To quantify axonal myelination, the G-ratio (the ratio of the inner axonal diameter to the total outer diameter) was determined for approximately 200 randomly selected fibers per group (~ 40 axons per mouse, 5 mice per group) using ImageJ software. In the statistical analysis of microglial lysosomes, we used Image J software to identify and quantify intracellular lysosomes (vesicles). Specifically, the number of vesicles in approximately five microglial cells per sample was individually counted, and the average value was calculated.

2.20 | Microglia Morphology Analysis

Microglial morphology was quantitatively analyzed from z-stack images of Iba1⁺ cells acquired using a confocal microscope (Olympus FV1000). For each mouse, 20–25 fields of view were randomly captured and analyzed. A series of morphological parameters, including soma area, soma volume, and sphericity were quantified using Imaris and ImageJ software. Sphericity was defined as a quantitative measure of how closely a cell approximates a perfect sphere, with a value of 1.0 indicating a perfect sphere. Sholl analysis assesses morphological complexity from a geometric perspective. This method involves superimposing a series of concentric circles centered on the cell body and calculating the intersection points between cellular processes (e.g., microglial cell branches) and each circle.

For skeleton analysis, maximum intensity projections of Iba1⁺ channels were generated from the z-stacks. The images were then inverted to 8-bit grayscale, and an Unsharp Mask filter (radius: 3 pixels) was applied to enhance contrast, followed by a despeckle step to reduce noise. The images were subsequently converted to binary format using an auto-threshold function, processed with binary closing and outlier removal functions to refine the structures, and finally skeletonized to enable the analysis of process architecture.

2.21 | Quantitative Real-Time PCR (qPCR)

Total RNA was isolated from primary microglia using Trizol reagent (Invitrogen). Complementary DNA (cDNA) was synthesized from the extracted RNA using the PrimeScript II First-Strand cDNA Synthesis Kit (Takara, RR036A), following the manufacturer's protocol. Quantitative PCR was performed using SYBR Green PCR Master Mix (Yeasen, 11201ES03) on a Bio-Rad Real-Time PCR system. Each sample was run in technical duplicates, and the relative expression of target genes was calculated using the 2^(-ΔΔCT) method[33]. All primer sequences used are listed in **Table S2**.

2.22 | Western Blot

Proteins were extracted from primary microglia, and quantified using the BCA Protein Assay kit (Boster, Ltd., Wuhan, China). Equal amounts of protein were separated on 10–15% SDS-PAGE gels and transferred to 0.45-μm nitrocellulose membranes. After blocked with 5% BSA, the membranes were incubated with primary antibodies at 4°C for more than 16 hours. After washed with TBST, membranes were incubated with secondary antibody (Jackson, USA) for 1 h at room temperature. The membranes

were visualized using an enhanced chemiluminescence kit (Advansta, USA, Cat#K-12043-D10). The bands were visualized with the Gelview 6000 pro system (BLT, China). The integrated optical densities (OD) were collected and analyzed with Image J.

2.23 | Statistical Analysis

Data are presented as the mean ± standard error of the mean (SEM), except for Luxol Fast Blue (LFB) scores, which are presented as the median with interquartile range. Statistical analyses were performed using GraphPad Prism software (version 8.0). Non-parametric data from LFB scoring were analyzed using the Mann-Whitney U test. Comparisons between two groups were conducted using a two-tailed Student's t-test, while comparisons among multiple groups were performed by one-way ANOVA followed by Tukey's post hoc test. A p-value of less than 0.05 was considered statistically significant.

3. Result

3.1 Chronic Cerebral Hypoperfusion Induces White Matter Injury and Lipid Droplet Accumulation in Microglia

A well-established bilateral common carotid artery stenosis (BCAS) mouse model was used to investigate the role of microglia in ischemic white matter injury induced by chronic cerebral hypoperfusion[34] (**Fig. S1A**). To validate successful model induction, cerebral blood flow (CBF) was measured by laser speckle flowmetry (LSF) before and after BCAS surgery. The results confirmed an approximate 40% reduction in CBF in wild-type mice following surgery (**Fig. S1B, C**). Furthermore, luxol fast blue (LFB) staining conducted one month after BCAS revealed substantial demyelination in several white matter regions, including the corpus callosum (CC), anterior commissure (AC), internal capsule (IC), and fimbria of the hippocampus (F). This was characterized by marked vacuolation and a significantly higher white matter lesion (WML) score compared to sham controls (**Fig. S1D, E**).

The pathological process of white matter injury involves loss of the myelin sheath and is accompanied by microglial activation. These activated microglia engulf lipid-rich myelin debris and sequester the derived lipids in intracellular lipid droplet (LD) [35]. Perilipin-2 (PLIN2), a major LD coat protein, serves as a surrogate marker of LD formation. As expected, immunofluorescence staining revealed a marked increase in $PLIN2^{+}Iba1^{+}$ cells in mice one month after BCAS (**Fig. S1F, G**). The above results indicate that chronic cerebral hypoperfusion promotes increased microglial engulfment of myelin and intracellular $PLIN2^{+}$LD accumulation, which may be critically involved in the pathophysiological process of demyelination.

3.2 Microglial *Plin2* Knockout Alleviates Cognitive Impairment and Anxiety-like Behavior in BCAS Mice

To further investigate the impact of microglial PLIN2 on white matter injury induced by chronic cerebral hypoperfusion, we subjected littermate controls (hereafter referred to as Control) and microglia-specific

Plin2$^{-/-}$ mice (hereafter referred to as *Plin2*$^{-/-}$) to the BCAS model (Fig. 1A). Microglia-specific *Plin2*$^{-/-}$ mice were generated and genotyped as previously described[9] (**Fig. S2**). A battery of behavioral tests, including the Morris water maze (MWM), novel object recognition (NOR), and open field test, was conducted from day 23 to day 30 after surgery to assess cognitive function and anxiety-like behavior (Fig. 1B). During the acquisition phase of the MWM, Control BCAS mice exhibited significantly prolonged escape latencies compared with sham controls, whereas *Plin2*$^{-/-}$ BCAS mice showed a marked attenuation of this learning deficit. In the probe test on day 6, *Plin2*$^{-/-}$ BCAS mice demonstrated a significant rescue of spatial memory, as evidenced by a shorter latency to reach the former platform location, increased platform crossings, and more time spent in the platform location compared to Control BCAS mice (Fig. 1C-E). In the NOR test (Fig. 1F), no significant differences in exploration time between two identical objects (A1 and A2) were observed among the groups during the familiarization phase (**Fig. S3A**), indicating the absence of innate object preference. During the test phase, Control BCAS mice showed a significantly reduced discrimination index versus sham controls, indicating impaired recognition memory, whereas this deficit was markedly attenuated in *Plin2*$^{-/-}$ BCAS mice (Fig. 1G, H).

In the open field test (Fig. 1I), Control BCAS mice exhibited reduced time spent in the central area, fewer central entries, and decreased numbers of grid crossings, accompanied by increased immobility time, compared with sham controls. These data indicated that the BCAS model induced anxiety-like behavior, diminished exploratory behavior, and reduced locomotor activity in mice, whereas these behavioral deficits were largely normalized in the Plin2$^{-/-}$ BCAS group (Fig. 1J and **Fig. S3B**).

Collectively, these results demonstrate that BCAS induces significant deficits in spatial learning and memory, as well as anxiety-like behavior, and that microglial *Plin2* deficiency effectively mitigates these impairments.

3.3 Microglial *Plin2* Deficiency Attenuates White Matter Injury and Promotes Remyelination after BCAS

To evaluate the impact of PLIN2 on chronic cerebral hypoperfusion injury, we assessed white matter integrity in the corpus callosum using LFB staining. The results showed that, following BCAS, *Plin2*$^{-/-}$ mice exhibited significantly less overall myelin sheath damage compared to Control mice. Consistently, BCAS-induced loss of myelin-associated glycoprotein (MAG) and myelin basic protein (MBP) was markedly attenuated in *Plin2*$^{-/-}$ mice, indicating reduced demyelination and better preservation of myelin sheath integrity (Fig. 2A, B and **Fig. S4**). We further examined the ultrastructure of myelin in the corpus callosum using transmission electron microscopy. Control BCAS mice exhibited fragmented myelin sheaths and prominent intramyelinic vacuolation, whereas *Plin2*$^{-/-}$ BCAS mice were largely protected from these ultrastructural abnormalities. Quantitative analysis of the G-ratio revealed a significant decrease in *Plin2*$^{-/-}$ mice compared to controls following BCAS, confirming that *Plin2* deletion greatly ameliorated myelin damage and was associated with relatively thicker myelin sheaths (Fig. 2C, D).

As the proliferation and maturation of oligodendrocytes are central to remyelination after white matter injury[36], we next quantified oligodendrocyte-lineage cells. Compared with the sham-operation group, BCAS led to a significant reduction in the densities of $Olig2^+$ cells (a generalized oligodendrocyte lineage marker) and $CC1^+$ cells (a mature oligodendrocyte marker) in Control mice. As expected, the density of mature oligodendrocytes was evidently higher in *Plin2*$^{-/-}$ BCAS mice than in Control BCAS mice. In addition, the density of $NG2^+$ cells, marking oligodendrocyte precursor cells (OPCs), was also markedly elevated in Plin2$^{-/-}$ mice versus Control mice subjected to BCAS (Fig. 2E, F), suggesting enhanced recruitment and proliferation of OPCs that may contribute to the remyelination process.

Overall, these findings demonstrate that microglial *Plin2* deficiency mitigates the severity of BCAS-induced demyelination by supporting oligodendrocyte lineage cell survival and promoting their maturation, thereby facilitating remyelination.

3.4 *Plin2* Deletion Alleviates Microglial Activation and Restores the Autophagy-Lysosomal Pathway in BCAS Mice

The functional phenotype of microglia is closely linked to white matter injury and cognitive impairment after chronic cerebral hypoperfusion[10, 37]. Activated microglia persistently secrete pro-inflammatory cytokines that suppress the differentiation of OPCs into mature oligodendrocytes, thereby impeding remyelination and exacerbating ischemic white matter injury[5]. We hypothesized that the neuroprotective effects observed in *Plin2*$^{-/-}$ mice following BCAS could be attributed to improved microglial function. To test this, we first analyzed microglial density and morphology. Quantitative 3D reconstruction using Imaris software revealed that, compared with sham controls, microglia in the corpus callosum of BCAS mice exhibited a marked increase in density, accompanied by a canonical activated phenotype—enlarged soma area and volume, as well as elevated sphericity and solidity—within lesion-associated regions. In contrast, conditional deletion of *Plin2* in microglia shifted their morphology toward a more ramified, resting-like state. Consistent with these observations, sholl analysis of microglial branching patterns further corroborated these phenotypic differences (Fig. 3A, B).

As the primary phagocytes in demyelinating lesions, microglia engulf myelin debris[38–40], which is subsequently converted into lipid droplets (LDs) and degraded via lipophagy (the autophagy-lysosomal pathway) and lipolysis[41]. To determine whether the LD coat protein PLIN2 regulates this degradative process, we performed co-immunostaining for the microglial marker Iba1 together with lysosomal (LAMP1) and autophagic (LC3B) markers. Compared with Control group, *Plin2* deficiency significantly attenuated the BCAS-induced accumulation of both LAMP1 and LC3B in microglia (Fig. 3C, D), suggesting a resolution of the impaired autophagy-lysosomal flux. We further assessed the ultrastructural features of this pathway using transmission electron microscopy. BCAS led to a notable accumulation of lysosomes in microglia, consistent with impaired clearance of myelin debris and LDs. This lysosomal buildup was evidently reduced in *Plin2*$^{-/-}$ mice compared to their Control littermates (Fig. 3E, F).

Taken together, our results indicate that *Plin2* deficiency mitigates microglial overactivation and alleviates defects in the autophagy-lysosomal pathway in myelin debris-engulfing microglia following BCAS.

3.5 *Plin2* Deficiency Reprograms Microglial Metabolic and Inflammatory Pathways after BCAS

To gain deeper mechanistic insight, we isolated microglia from white matter lesions of mice in different groups using FACS, and performed transcriptomic profiling via the high-resolution Smart-seq2 technique[42](Fig. 4A and **Fig. S5**). The volcano plot of differentially expressed genes (DEGs) highlighted extensive transcriptional differences between the Control BCAS and *Plin2*$^{-/-}$ BCAS groups, indicating that *Plin2* deletion markedly remodels the brain transcriptional landscape in the BCAS model (**Fig. S6**).

We identified 661 DEGs between the Control Sham and Control BCAS groups, and 668 DEGs between the Control BCAS and *Plin2*$^{-/-}$ BCAS groups, of which 277 genes were shared between the two comparisons (Fig. 4B). GO and KEGG pathway enrichment analyses of these 277 shared DEGs showed their primary involvement in metabolic reprogramming, immune and inflammatory regulation. Notably, pathways related to cytokine and chemokine regulation were among the most significantly enriched, while lipid metabolism and autophagy-related terms showed the highest gene counts and enrichment scores (Fig. 4C). The circular heatmap further displayed the expression patterns of genes involved in the processes of lipophagy, phagocytosis, inflammation, and chemotaxis cross the different groups (Fig. 4D). This implies that *Plin2* deficiency facilitates white matter repair after BCAS possibly by modulating the above specific pathways.

To further elucidate how *Plin2* deletion remodels pathway-level responses, we performed gene set enrichment analysis (GSEA). As illustrated in the pathway enrichment bubble plot, gene sets associated with lysosomal activation, autophagy induction, inflammatory response, and innate immune responses were negatively enriched, whereas gene sets associated with long-chain fatty acid metabolism, ATP biosynthesis, and PPAR signaling were significantly enriched in *Plin2*$^{-/-}$ BCAS microglia compared to Control BCAS microglia (Fig. 4E). The GSEA running enrichment score plots further provided an intuitive visualization of the enrichment patterns of these pathway-related gene sets in *Plin2*$^{-/-}$ BCAS microglia (Fig. 4F).

Collectively, these findings suggest that *Plin2* deficiency reshapes the adaptive responses of microglia following BCAS, likely through reprogramming lipid and energy metabolism pathways.

3.6 *Plin2* Deficiency Reduces Lipid Droplet Accumulation and Reprograms Lipid Metabolism in Myelin Debris-Engulfing Microglia

Building on our *in vivo* findings that *Plin2* deletion modulates lipid metabolism and alleviates microglial activation, we next sought to delineate the specific molecular mechanisms by which PLIN2 regulates

lipid profiles and inflammatory responses in myelin debris-exposed microglia *in vitro*. To characterize microglial responses at distinct sequential stages of myelin processing, we first performed siRNA-mediated knockdown of *Plin2* in primary microglia, and then exposed the cells to myelin debris for varying durations to mimic the progressive course of demyelination (Fig. 5A). Microglia effectively engulfed abundant myelin debris, leading to the formation of $BODIPY^{+}PLIN2^{+}$ LDs (**Fig. S7A**). Western blot analysis confirmed efficient *Plin2* knockdown (**Fig. S7B**). First, we dynamically monitored microglial phagocytosis of myelin debris. Notably, *Plin2* knockdown did not affect microglial phagocytic capacity, as indicated by comparable mean fluorescence intensities of PKH26-labeled myelin in cells and supernatants among the groups (**Fig. S7C**).

Given that microglia phagocytose myelin debris and convert it into intracellular LDs[43, 44], we next tracked LD dynamics. Flow cytometry and BODIPY staining revealed that exposure to myelin debris markedly increased LD levels in microglia, whereas *Plin2* knockdown greatly reduced LD accumulation at both 24 h and 48 h, with a more pronounced reduction at 48 h (Fig. 5B-E). To gain deeper insight into the lipid metabolic alterations, we performed lipidomic analysis at 48 hours across the different groups. After 48 h of exposure to myelin debris, levels of free fatty acids (FAs) and multiple neutral lipid species, including diacylglycerols (DG), monoacylglycerols (MG), and cholesteryl esters (CE), were markedly increased in microglia, further corroborating the LD accumulation described above. In contrast, *Plin2*-targeting siRNA (si-*Plin2*)-transfected microglia exhibited significantly reduced levels of these metabolites compared with the non-targeting control siRNA (si-NC) group, suggesting that *Plin2* knockdown accelerated lipid degradation within LDs and alleviated the excessive lipid metabolic burden in microglia (Fig. 5F).

3.7 *Plin2* Deficiency Attenuates Microglial Inflammation by Promoting Lipid Droplet Catabolism via Coordinated Lipophagy and Lipolysis

LD degradation occurs primarily through two fundamental pathways: lipolysis, mediated by cytosolic lipases, and lipophagy, which involves the autophagy-lysosomal cascade[45]. We therefore hypothesized that the reduction in LDs observed upon *Plin2* knockdown results from coordinated activation of both lipolytic and lipophagic pathways. To monitor LD degradation over time, samples were collected at multiple time points after myelin debris exposure, at which the expression of lysosomal (LAMP1) and autophagic (LC3B) markers, as well as key lipases, was assessed. At 8 h and 24 h after myelin debris exposure, *Plin2* knockdown markedly enhanced activation of the autophagy-lysosomal pathway compared with si-NC group, as evidenced by increased LAMP1 and LC3B expression, consistent with more efficient degradation of LD-stored lipids. By 48 h, expression of these markers, particularly LAMP1, declined in the si-*Plin2* group, likely reflecting the resolution of the autophagic response following completion of lipid clearance (Fig. 6A, 6B, and **Fig. S8**). At the 24 h time point after myelin exposure, the results of qPCR demonstrated that *Plin2* knockdown led to a prominent increase in the mRNA levels of lipases involved in lipolysis, including adipose triglyceride lipase (ATGL), hormone-sensitive lipase (HSL),

monoacylglycerol lipase (MGL), lysosomal acid lipase A (LIPA), and lipoprotein lipase (LPL), which indicated a concurrent activation of the lipolytic pathway (Fig. 6C).

Given the established link between LD accumulation and pro-inflammatory microglial phenotype[30, 46], we hypothesized that accelerated LD catabolism upon *Plin2* deletion would attenuate inflammation. To assess this, microglia were stimulated with myelin debris in combination with LPS to better mimic the inflammatory milieu following demyelination (Fig. 6D). As expected, *Plin2* knockdown significantly attenuated the pro-inflammatory microglial phenotype induced by myelin debris and LPS compared with the si-NC group, as evidenced by reduced mRNA levels of pro-inflammatory mediators IL-1β, IL-6, TNF-α, and iNOS. In parallel, expression of anti-inflammatory markers such as Arg1 was increased in si-*Plin2*-transfected microglia, suggesting a shift from a pro-inflammatory toward an anti-inflammatory microglial phenotype (Fig. 6E). Taken together, these results indicate that *Plin2* deficiency alleviates microglial inflammatory responses, likely by enhancing LD clearance and reprogramming lipid metabolism.

3.8 Inhibition of Autophagy Reverses the Neuroprotective effect of *Plin2* Deficiency

Our data indicate that *Plin2* deletion protects against chronic cerebral hypoperfusion by enhancing microglial autophagy-lysosomal flux and promoting clearance of myelin-derived LDs. To determine whether this protection is autophagy-dependent, we administered the lysosomal autophagy inhibitor CQ to *Plin2*$^{-/-}$ mice subjected to BCAS.

As outlined in Fig. 7A, *Plin2*$^{-/-}$ mice received daily intraperitoneal injections of CQ following BCAS surgery until day 30. Behavioral assessments, including the MWM and TreadScan gait analysis, were performed from day 23 to 30 after surgery. In the MWM acquisition phase, CQ treatment abolished the improved spatial learning typically observed in *Plin2*$^{-/-}$ BCAS mice relative to Control BCAS mice (Fig. 7B). During the probe test, CQ-treated *Plin2*$^{-/-}$ BCAS mice exhibited significantly longer escape latency and less time in the platform location compared to their vehicle-treated *Plin2*$^{-/-}$ BCAS counterparts (Fig. 7C, D), indicating that autophagy inhibition reversed the cognitive benefits conferred by *Plin2* deletion. Gait analysis further supported this reversal, as a cluster heatmap of key mobility parameters showed that CQ-treated *Plin2*$^{-/-}$ BCAS mice clustered distinctly from vehicle-treated *Plin2*$^{-/-}$ BCAS mice but closely with Control BCAS mice (Fig. 7E). Specifically, the *Plin2*$^{-/-}$ BCAS + CQ group exhibited significantly lower RRInsideQuad3, FR PrintAngle2, FROutsideQuad2, FL Avg StrideTime, LeftWallHugDist, and LateralPos values compared with the *Plin2*$^{-/-}$ BCAS group (Fig. 7F and **Fig. S9**). As shown in the PLS-DA plot (Fig. 7G), the profile of *Plin2*$^{-/-}$ BCAS group was clearly separated from the Control BCAS group, whereas the *Plin2*$^{-/-}$ BCAS + CQ group clustered closer to the Control BCAS group. The above analyses confirmed that CQ-induced autophagy inhibition partially abrogated the protective effects of *Plin2* deletion on BCAS-induced gait disturbances and motor deficits. Consistent with the behavioral data, the neuropathological benefits conferred by *Plin2* deficiency were largely abrogated by CQ. While *Plin2*$^{-/-}$ BCAS mice showed reduced white matter injury, additional CQ treatment significantly reversed this

improvement, as evidenced by higher white matter lesions score in LFB staining and decreased immunoreactivity for myelin protein MAG (Fig. 7H, I). Quantitative and morphological analyses of microglia revealed that CQ administration partially abrogated the ramified, resting-like phenotype observed in *Plin2*$^{-/-}$ BCAS mice, leading to increased microglial activation (Fig. 7J, K).

In vitro, treatment of *Plin2*-knockdown primary microglia with CQ after myelin debris exposure abolished the accelerated lipid clearance observed in these cells, resulting in significant lipid droplet accumulation (Fig. 8A-D). This indicates that the enhanced lipid degradation upon *Plin2* knockdown is dependent on an intact autophagy-lysosomal pathway. Furthermore, to evaluate microglial inflammatory responses, we stimulated cells with myelin debris plus LPS. Based on morphological assessment and quantification of pro-inflammatory markers (TNF-α, IL-1β, IL-6, and iNOS), *Plin2*-depleted microglia predominantly exhibited a ramified, resting-like phenotype rather than a pro-inflammatory amoeboid morphology, with significantly reduced production of these cytokines compared with the si-NC group. In sharp contrast, treatment with CQ largely abrogated the anti-inflammatory phenotype of *Plin2*$^{-/-}$ microglia under inflammatory stimulation (Fig. 8E-G).

Overall, CQ-mediated autophagy inhibition largely abolished the cognitive, gait, and white-matter benefits conferred by *Plin2* deletion after BCAS, accompanied by increased microglial activation. Consistently, CQ treatment blocked the *Plin2* knockdown-induced enhancement of autophagy-lysosomal pathway-mediated LD clearance *in vitro*, leading to LD accumulation and a restored pro-inflammatory phenotype.

4. Discussion

To the best of our knowledge, this study is the first to elucidate the protective role of microglial *Plin2* deletion in chronic cerebral hypoperfusion-induced white matter injury and its mechanistic basis. Our key findings are as follows: (1) Microglia-specific *Plin2* knockout alleviated cognitive deficits and gait dysfunction in BCAS mice. (2) Microglia-specific *Plin2* deficiency attenuated demyelinating lesions, as evidenced by promoted oligodendrocyte regeneration and remyelination. (3) Mechanistically, *Plin2* deletion reprogrammed microglial lipid metabolism, facilitated LD clearance, and thereby shifted microglia from a pro-inflammatory to a homeostatic phenotype, creating a permissive microenvironment for remyelination. (4) The neuroprotective effects were dependent on restoration of the autophagy-lysosomal pathway (lipophagy), as pharmacological inhibition of autophagy reversed the benefits conferred by *Plin2* knockout. A schematic summary of these findings is provided in the graphical abstract (Fig. 8H).

After demyelination, the multiplication and differentiation of OPCs contribute to the effective myelin regeneration[47]. Kotter et al. pointed out that myelin debris inhibited the differentiation of OPCs into mature myelinated oligodendrocytes (OLs)[48, 49]. Therefore, the timely clearance of excessive myelin debris by phagocytes, primarily microglia, is a critical prerequisite for successful remyelination[11, 50]. Microglia maintain CNS homeostasis by phagocytosing damaged myelin, but an overload of engulfed debris can lead to dysfunction of the autophagy-lysosomal pathway and subsequent LD

accumulation[11]. Moreover, microglial activation states are tightly coupled to the dynamic balance between demyelination and remyelination[29]. Classically activated (pro-inflammatory) microglia secrete abundant inflammatory cytokines that inhibit OPC differentiation, whereas microglia in a homeostatic state support this process by releasing various trophic factors[51]. In brief, effective repair of demyelinating lesions requires both efficient clearance of cholesterol-rich myelin debris and a shift from a pro-inflammatory to an anti-inflammatory microenvironment[52]. Consistent with this paradigm, our study demonstrates that *Plin2* knockout markedly promotes the repair of demyelinating lesions following ischemic white matter injury, as reflected by enhanced oligodendrocyte regeneration and attenuation of the microglial activation-mediated inflammatory milieu.

Once internalized by microglia, myelin is processed within lysosomes, generating free cholesterol and fatty acids. When present in excess, these lipids are esterified and stored as cholesteryl esters and triacylglycerols in cytoplasmic LDs[53]. This sequestration not only protects microglia from lipotoxicity but also establishes a reservoir of non-toxic, esterified lipids[54]. PLIN2, a major LD coat protein, plays a pivotal role in stabilizing LDs by shielding their neutral lipid core from cytosolic lipases, thereby limiting lipid turnover[41]. PLIN2 regulates LD metabolism through two primary pathways. First, PLIN2 inhibits fat breakdown by directly binding to lipases such as ATGL at the LD surface, where it forms a spatial barrier that blocks the access of lipases to their substrates (triglycerides). The absence of PLIN2 relieves this inhibition, thereby enhancing lipolysis-mediated LD turnover and reducing lipid storage in macrophages[9]. Second, PLIN2 modulates LD degradation via the autophagy-lysosomal pathway (lipophagy, a selective autophagy subtype targeting LDs). By shielding the droplet surface, PLIN2 prevents recognition and sequestration by autophagic machinery (e.g., LC3, Rab7). Its depletion removes this barrier, promoting autophagy-dependent catabolism of triglycerides and cholesterol esters, ultimately decreasing intracellular LD accumulation[55, 56]. While studies of diabetes-related cognitive decline have shown that inhibition of lipophagy leads to LD accumulation in microglia [57], it has remained unclear whether microglial PLIN2 participates in LD-mediated lipid metabolism in the context of BCAS-induced white matter injury. Our *in vivo* experiments and *in vitro* lipid metabolomics analyses demonstrate that *Plin2* knockout promotes the degradation of cholesteryl esters and triglycerides via lipophagy and lipase-mediated pathways, thereby preventing LD accumulation within microglia. Collectively, *Plin2* deficiency ameliorates BCAS-induced ischemic white matter injury and cognitive deficits by modulating post-phagocytic reprogramming of lipid metabolism in myelin-engulfing microglia.

Dysregulation of the autophagy-lysosomal process is a common feature across a wide spectrum of neurological diseases. However, autophagy-mediated regulation of microglial responses is highly context-dependent and involves considerable mechanistic complexity. On the one hand, enhancing autophagy has been proven to exert neuroprotective effects in neurodegenerative disease models. Experimental evidence demonstrates that autophagy activation restricts NLRP3 inflammasome accumulation in microglia during Alzheimer’s disease (AD)[58]. Moreover, in multiple sclerosis, autophagy activation restores impaired autophagic flux, attenuates the pro-inflammatory microglial phenotype, and consequently exerts a neuroprotective effect[59]. On the other hand, excessive or sustained activation of autophagy may have counterproductive effects and even become detrimental.

During severe demyelination, aberrant overactivation of autophagy drives excessive delivery of lipid substrates to lysosomes, resulting in microglial dysfunction and a shift toward a pro-inflammatory phenotype[27]. Taken together, these findings indicate that both overactivation and insufficient activation of autophagy can reshape the inflammatory phenotype of microglia, underscoring the importance of finely tuned and dynamic autophagy regulation in maintaining microglial functional states, likely through autophagy-mediated control of microglial metabolic pathways[60]. Thus, therapeutic strategies targeting autophagy in microglia will need to achieve precise and temporally controlled modulation. To our knowledge, this is the first study to demonstrate that, in a chronic cerebral hypoperfusion-induced white matter injury model, *Plin2* deletion restores the impaired autophagy-lysosomal pathway in microglia, thereby attenuating their pro-inflammatory phenotype and ultimately facilitating remyelination.

Notably, in our *in vivo* model, the neuroprotective effects of *Plin2* knockdown were linked to the restoration of autophagy-lysosomal function. In contrast, our *in vitro* experiments demonstrate that activation of this pathway promotes LD clearance in the absence of PLIN2, thereby mitigating inflammatory responses, whereas autophagy inhibition abolishes this benefit. We therefore propose a dynamic, two-phase framework linking microglial autophagy-lysosomal regulation to lipid metabolism and inflammatory remodeling. In the initial phase following myelin phagocytosis, PLIN2 acts as a brake on lipophagy. PLIN2-sufficient microglia exhibit restrained autophagic activation, leading to progressive LD accumulation. By contrast, PLIN2-deficient microglia mount a rapid and robust autophagic response that effectively clears LDs at an early stage. This early clearance is crucial, as it partially prevents the subsequent transition to a chronic state of lipid overload. Consequently, in the later phase, once lipid overload has been effectively relieved, the autophagic response in *Plin2*-deficient microglia returns toward a healthier functional baseline, thereby resolving inflammation and creating a permissive environment for oligodendrocyte differentiation and remyelination. The causal contribution of lipophagy to this protective cascade is further supported by our CQ inhibition experiments. Pharmacological blockade of the autophagy-lysosomal pathway exacerbated LD accumulation and abolished the protective effects of *Plin2* knockout, indicating that this phenotype critically depends on an intact lipophagic flux.

This study has several limitations that warrant consideration. First, we focused exclusively on microglial PLIN2 and did not examine its roles in oligodendrocytes or astrocytes. Cell type-specific knockout models will be required to clarify the contribution of PLIN2 to LD metabolism and white matter repair in these glial populations. Second, CQ inhibits autophagy globally and may exert off-target effects on lysosomal function. Future studies employing microglia-specific Atg5 or Atg7 knockout mice are needed to more precisely define the cell-autonomous contribution of autophagy. Finally, we did not investigate direct interactions between PLIN2 and autophagy-related proteins. Co-immunoprecipitation experiments will be necessary to determine whether PLIN2 blocks autophagic LD degradation by binding these proteins.

Conclusion

In conclusion, our study demonstrates that microglial *Plin2* deficiency confers significant protection against cognitive deficits, gait disturbances, and demyelinating lesions in a mouse model of ischemic white matter injury. Mechanistically, loss of PLIN2 facilitates lipid metabolism in myelin-engulfing microglia by enhancing lipophagy and lipase-mediated lipolysis, thereby alleviating microglia-mediated neuroinflammation and ultimately promoting remyelination. From a clinical perspective, PLIN2 might serve as a promising therapeutic target for ischemic white matter injury and vascular cognitive impairment.

Abbreviations

VCI	Vascular cognitive impairment
PLIN2	Perilipin-2
OPCs	Oligodendrocyte precursor cells
CNS	Central nervous system
LDs	Lipid droplets
TG	Triglyceride
BCAS	Bilateral common carotid artery stenosis
CBF	Cerebral blood flow
LFB	Luxol fast blue
WML	White matter lesion
MAG	Myelin-associated glycoprotein
MBP	Myelin basic protein
MWM	Morris water maze
NOR	Novel object recognition
OFT	Open field test
FACS	Fluorescence-Activated Cell Sorting
DEGs	Differentially expressed genes
GO	Gene Ontology
KEGG	Kyoto Encyclopedia of Genes and Genomes
GSEA	Gene Set Enrichment Analysis
FAs	Free fatty acids
DG	Diacylglycerols
MG	Monoacylglycerols
CE	Cholesteryl esters
ATGL	Adipose triglyceride lipase
HSL	Hormone-sensitive lipase
MGL	Monoacylglycerol lipase
LIPA	Lysosomal acid lipase A
LPL	Lipoprotein lipase

LPS	Lipopolysaccharide
CQ	Chloroquine
PLS-DA	Partial least squares discriminant analysis

Declarations

Ethics approval and consent to participate

This study was approved by the Institutional Animal Care and Use Committee of Tongji Hospital, Tongji Medical College, Huazhong University of Science and Technology (Permit Number: TJH-202304028). All animal experiments were performed in accordance with the institutional guidelines and national ethical regulations for animal research.

Consent for publication

Not applicable

Availability of data and materials

The datasets generated and/or analysed during the current study are not publicly available due to internal experimental data protection restrictions but are available from the corresponding author on reasonable request.

Competing interests

Not applicable

Funding

Ministry of Science and Technology China Brain Initiative Grant 2022ZD0204704 (W. Wang)

National Natural Science Foundation of China 82301507 (Y. Xie)

Nature Science Foundation of Hubei Province 2025AFB574 (Y. Xie)

Major research program of National Natural Science Foundation 92248304 (W. Wang)

Authors' contributions

Conceptualization: YX, XYW, WW

Methodology: XYW, YX, MJX

Investigation: XYW, YX, ZYH, HZ, SL

Visualization: XYW

Supervision: MJX, ZYY

Writing—original draft: XYW

Writing—review & editing: YX

Acknowledgements

We acknowledge Dr. Masunari Shibata for establishing the stable bilateral common carotid artery stenosis (BCAS) model, and kindly providing technical details.

References

1. van der Flier WM, Skoog I, Schneider JA, Pantoni L, Mok V, Chen CLH, Scheltens P. Vascular cognitive impairment. Nat Rev Dis Primers. 2018;4:18003.
2. Rajeev V, Fann DY, Dinh QN, Kim HA, De Silva TM, Lai MKP, Chen CL, Drummond GR, Sobey CG, Arumugam TV. Pathophysiology of blood brain barrier dysfunction during chronic cerebral hypoperfusion in vascular cognitive impairment. Theranostics. 2022;12:1639–58.
3. Iadecola C, Duering M, Hachinski V, Joutel A, Pendlebury ST, Schneider JA, Dichgans M. Vascular Cognitive Impairment and Dementia: JACC Scientific Expert Panel. J Am Coll Cardiol. 2019;73:3326–44.
4. Zhang LY, Pan J, Mamtilahun M, Zhu Y, Wang L, Venkatesh A, Shi R, Tu X, Jin K, Wang Y, et al. Microglia exacerbate white matter injury via complement C3/C3aR pathway after hypoperfusion. Theranostics. 2020;10:74–90.
5. Berghoff SA, Spieth L, Sun T, Hosang L, Schlaphoff L, Depp C, Düking T, Winchenbach J, Neuber J, Ewers D, et al. Microglia facilitate repair of demyelinated lesions via post-squalene sterol synthesis. Nat Neurosci. 2021;24:47–60.
6. Ghorbani S, Yong VW. The extracellular matrix as modifier of neuroinflammation and remyelination in multiple sclerosis. Brain. 2021;144:1958–73.
7. Wang N, Wang M, Jeevaratnam S, Rosenberg C, Ikezu TC, Shue F, Doss SV, Alnobani A, Martens YA, Wren M, et al. Opposing effects of apoE2 and apoE4 on microglial activation and lipid metabolism in response to demyelination. Mol Neurodegener. 2022;17:75.
8. Prinz M, Jung S, Priller J. Microglia Biology: One Century of Evolving Concepts. Cell. 2019;179:292–311.
9. Loix M, Wouters E, Vanherle S, Dehairs J, McManaman JL, Kemps H, Swinnen JV, Haidar M, Bogie JFJ, Hendriks JJA. Perilipin-2 limits remyelination by preventing lipid droplet degradation. Cell Mol Life Sci. 2022;79:515.

10. Bogie JFJ, Haidar M, Kooij G, Hendriks JJA. Fatty acid metabolism in the progression and resolution of CNS disorders. Adv Drug Deliv Rev. 2020;159:198–213.
11. Haidar M, Loix M, Vanherle S, Dierckx T, Vangansewinkel T, Gervois P, Wolfs E, Lambrichts I, Bogie JFJ, Hendriks JJA. Targeting lipophagy in macrophages improves repair in multiple sclerosis. Autophagy. 2022;18:2697–710.
12. Shiffman D, Mikita T, Tai JT, Wade DP, Porter JG, Seilhamer JJ, Somogyi R, Liang S, Lawn RM. Large scale gene expression analysis of cholesterol-loaded macrophages. J Biol Chem. 2000;275:37324–32.
13. Paul A, Chang BH, Li L, Yechoor VK, Chan L. Deficiency of adipose differentiation-related protein impairs foam cell formation and protects against atherosclerosis. Circ Res. 2008;102:1492–501.
14. Tsai TH, Chen E, Li L, Saha P, Lee HJ, Huang LS, Shelness GS, Chan L, Chang BH. The constitutive lipid droplet protein PLIN2 regulates autophagy in liver. Autophagy. 2017;13:1130–44.
15. Percie du Sert N, Ahluwalia A, Alam S, Avey MT, Baker M, Browne WJ, Clark A, Cuthill IC, Dirnagl U, Emerson M, et al. Reporting animal research: Explanation and elaboration for the ARRIVE guidelines 2.0. PLoS Biol. 2020;18:e3000411.
16. Qin C, Liu Q, Hu ZW, Zhou LQ, Shang K, Bosco DB, Wu LJ, Tian DS, Wang W. Microglial TLR4-dependent autophagy induces ischemic white matter damage via STAT1/6 pathway. Theranostics. 2018;8:5434–51.
17. Chen C, Yang C, Wang J, Huang X, Yu H, Li S, Li S, Zhang Z, Liu J, Yang X, Liu GP. Melatonin ameliorates cognitive deficits through improving mitophagy in a mouse model of Alzheimer's disease. J Pineal Res. 2021;71:e12774.
18. Vorhees CV, Williams MT. Morris water maze: procedures for assessing spatial and related forms of learning and memory. Nat Protoc. 2006;1:848–58.
19. Qin C, Chen M, Dong MH, Yang S, Zhang H, You YF, Zhou LQ, Chu YH, Tang Y, Pang XW, et al. Soluble TREM2 triggers microglial dysfunction in neuromyelitis optica spectrum disorders. Brain. 2024;147:163–76.
20. Ritchie TM, Feng E, Vahedi F, Ermolina S, Bellissimo CJ, De Jong E, Portillo AL, Poznanski SM, Chan L, Ettehadieh SM, et al. The impact of oral cannabis consumption during pregnancy on maternal spiral artery remodelling, fetal growth and offspring behaviour in mice. EBioMedicine. 2025;114:105572.
21. Xie Y, Chen X, Li Y, Chen S, Liu S, Yu Z, Wang W. Transforming growth factor-beta1 protects against LPC-induced cognitive deficit by attenuating pyroptosis of microglia via NF-kappaB/ERK1/2 pathways. J Neuroinflammation. 2022;19:194.
22. Manley NC, Priest CA, Denham J, Wirth ED 3rd, Lebkowski JS. Human Embryonic Stem Cell-Derived Oligodendrocyte Progenitor Cells: Preclinical Efficacy and Safety in Cervical Spinal Cord Injury. Stem Cells Transl Med. 2017;6:1917–29.
23. Zhang H, Yang S, Chen M, Tian DS, Qin C. Isolation of Mouse Primary Microglia by Magnetic-Activated Cell Sorting in Animal Models of Demyelination. J Vis Exp 2022.

24. Qin C, Yang S, Chen M, Dong MH, Zhou LQ, Chu YH, Shen ZX, Bosco DB, Wu LJ, Tian DS, Wang W. Modulation of microglial metabolism facilitates regeneration in demyelination. iScience. 2023;26:106588.
25. Serdar M, Herz J, Kempe K, Lumpe K, Reinboth BS, Sizonenko SV, Hou X, Herrmann R, Hadamitzky M, Heumann R, et al. Fingolimod protects against neonatal white matter damage and long-term cognitive deficits caused by hyperoxia. Brain Behav Immun. 2016;52:106–19.
26. Peng S, Su P, Liu L, Li Z, Liu Y, Tian L, Bai M, Xu E, Li Y. Formononetin ameliorates depression-like behaviors through rebalancing microglia M1/M2 polarization and inhibiting NLRP3 inflammasome: involvement of activating PPARα-mediated autophagy. Mol Med. 2025;31:153.
27. Zhou LQ, Dong MH, Hu ZW, Tang Y, Chu YH, Chen M, Yang S, Chen Z, Wu LJ, Wang W, et al. Staged suppression of microglial autophagy facilitates regeneration in CNS demyelination by enhancing the production of linoleic acid. Proc Natl Acad Sci U S A. 2023;120:e2209990120.
28. Qiu B, Simon MC. BODIPY 493/503 Staining of Neutral Lipid Droplets for Microscopy and Quantification by Flow Cytometry. Bio Protoc 2016, 6.
29. Qin C, Chu YH, Zhou LQ, Dong MH, Wang W, Tian DS. Haste makes waste: staged suppression of autophagic-lysosomal pathway in microglia promotes the efficient clearance of myelin debris. Autophagy. 2023;19:1896–8.
30. Marschallinger J, Iram T, Zardeneta M, Lee SE, Lehallier B, Haney MS, Pluvinage JV, Mathur V, Hahn O, Morgens DW, et al. Lipid-droplet-accumulating microglia represent a dysfunctional and proinflammatory state in the aging brain. Nat Neurosci. 2020;23:194–208.
31. Xie Y, Chen X, Wang X, Liu S, Chen S, Yu Z, Wang W. Transforming growth factor-beta1 protects against white matter injury and reactive astrogliosis via the p38 MAPK pathway in rodent demyelinating model. J Neurochem. 2024;168:83–99.
32. Shibata M, Ohtani R, Ihara M, Tomimoto H. White matter lesions and glial activation in a novel mouse model of chronic cerebral hypoperfusion. Stroke. 2004;35:2598–603.
33. Buechler C, Ritter M, Duong CQ, Orso E, Kapinsky M, Schmitz G. Adipophilin is a sensitive marker for lipid loading in human blood monocytes. Biochim Biophys Acta. 2001;1532:97–104.
34. Ihara M, Tomimoto H. Lessons from a mouse model characterizing features of vascular cognitive impairment with white matter changes. J Aging Res. 2011;2011:978761.
35. Gouna G, Klose C, Bosch-Queralt M, Liu L, Gokce O, Schifferer M, Cantuti-Castelvetri L, Simons M. TREM2-dependent lipid droplet biogenesis in phagocytes is required for remyelination. J Exp Med 2021, 218.
36. Mecha M, Yanguas-Casas N, Feliu A, Mestre L, Carrillo-Salinas F, Azcoitia I, Yong VW, Guaza C. The endocannabinoid 2-AG enhances spontaneous remyelination by targeting microglia. Brain Behav Immun. 2019;77:110–26.
37. Pang XW, Chu YH, Zhou LQ, Chen M, You YF, Tang Y, Yang S, Zhang H, Xiao J, Deng G, et al. Trem2 deficiency attenuates microglial phagocytosis and autophagic-lysosomal activation in white matter hypoperfusion. J Neurochem. 2023;167:489–504.

38. You YF, Chen M, Tang Y, Yu WX, Pang XW, Chu YH, Zhang H, Shang K, Deng G, Zhou LQ, et al. TREM2 deficiency inhibits microglial activation and aggravates demyelinating injury in neuromyelitis optica spectrum disorder. J Neuroinflammation. 2023;20:89.
39. Wei W, Lattau SSJ, Xin W, Pan Y, Tatenhorst L, Zhang L, Graf I, Kuang Y, Zheng X, Hao Z, et al. Dynamic Brain Lipid Profiles Modulate Microglial Lipid Droplet Accumulation and Inflammation Under Ischemic Conditions in Mice. Adv Sci (Weinh). 2024;11:e2306863.
40. Ou Z, Cheng Y, Ma H, Chen K, Lin Q, Chen J, Guo R, Huang Z, Cheng Q, Alaeiilkhchi N, et al. miR-223 accelerates lipid droplets clearance in microglia following spinal cord injury by upregulating ABCA1. J Transl Med. 2024;22:659.
41. Corbo JH, Chung J. Mechanisms of lipid droplet degradation. Curr Opin Cell Biol. 2024;90:102402.
42. Zhang H, Zhou LQ, Yang S, Dong MH, Chen L, Lu YL, Zhang LY, Zhang L, Chu YH, Xu LL, et al. The foam cell-derived exosomes exacerbate ischemic white matter injury via transmitting metabolic defects to microglia. Cell Metab. 2025;37:1636–e16541610.
43. Nugent AA, Lin K, van Lengerich B, Lianoglou S, Przybyla L, Davis SS, Llapashtica C, Wang J, Kim DJ, Xia D, et al. TREM2 Regulates Microglial Cholesterol Metabolism upon Chronic Phagocytic Challenge. Neuron. 2020;105:837–e854839.
44. Hammel G, Zivkovic S, Ayazi M, Ren Y. Consequences and mechanisms of myelin debris uptake and processing by cells in the central nervous system. Cell Immunol. 2022;380:104591.
45. Kloska A, Wesierska M, Malinowska M, Gabig-Ciminska M, Jakobkiewicz-Banecka J. Lipophagy and Lipolysis Status in Lipid Storage and Lipid Metabolism Diseases. Int J Mol Sci 2020, 21.
46. Liu Y, Wu C, Hou Z, Fu X, Yuan L, Sun S, Zhang H, Yang D, Yao X, Yang J. Pseudoginsenoside-F11 Accelerates Microglial Phagocytosis of Myelin Debris and Attenuates Cerebral Ischemic Injury Through Complement Receptor 3. Neuroscience. 2020;426:33–49.
47. Baaklini CS, Ho MFS, Lange T, Hammond BP, Panda SP, Zirngibl M, Zia S, Himmelsbach K, Rana H, Phillips B et al. Microglia promote remyelination independent of their role in clearing myelin debris. Cell Rep 2023, 42.
48. Kotter MR, Li WW, Zhao C, Franklin RJ. Myelin impairs CNS remyelination by inhibiting oligodendrocyte precursor cell differentiation. J Neurosci. 2006;26:328–32.
49. Kotter MR, Zhao C, van Rooijen N, Franklin RJ. Macrophage-depletion induced impairment of experimental CNS remyelination is associated with a reduced oligodendrocyte progenitor cell response and altered growth factor expression. Neurobiol Dis. 2005;18:166–75.
50. Safaiyan S, Kannaiyan N, Snaidero N, Brioschi S, Biber K, Yona S, Edinger AL, Jung S, Rossner MJ, Simons M. Age-related myelin degradation burdens the clearance function of microglia during aging. Nat Neurosci. 2016;19:995–8.
51. Psenicka MW, Smith BC, Tinkey RA, Williams JL. Connecting Neuroinflammation and Neurodegeneration in Multiple Sclerosis: Are Oligodendrocyte Precursor Cells a Nexus of Disease? Front Cell Neurosci. 2021;15:654284.

52. Kuhlmann T, Ludwin S, Prat A, Antel J, Brück W, Lassmann H. An updated histological classification system for multiple sclerosis lesions. Acta Neuropathol. 2016;133:13–24.
53. Olzmann JA, Carvalho P. Dynamics and functions of lipid droplets. Nat Rev Mol Cell Biol. 2019;20:137–55.
54. Walther TC, Chung J, Farese RV Jr.. Lipid Droplet Biogenesis. Annu Rev Cell Dev Biol. 2017;33:491–510.
55. Sztalryd C, Brasaemle DL. The perilipin family of lipid droplet proteins: Gatekeepers of intracellular lipolysis. Biochim Biophys Acta Mol Cell Biol Lipids. 2017;1862:1221–32.
56. Hua Z, Li X, Yu L, Qian J, Tian M, Bai X, Yang J, Deng R, Liu Q, Lu C et al. Liver-targeting exosomes loaded naringenin ameliorate metabolic dysfunction-associated steatotic liver disease through ubiquitin-proteasome system initiated lipophagy. Chem Eng J 2025, 523.
57. Li Q, Zhao Y, Guo H, Li Q, Yan C, Li Y, He S, Wang N, Wang Q. Impaired lipophagy induced-microglial lipid droplets accumulation contributes to the buildup of TREM1 in diabetes-associated cognitive impairment. Autophagy. 2023;19:2639–56.
58. Jha D, Bakker E, Kumar R. Mechanistic and therapeutic role of NLRP3 inflammasome in the pathogenesis of Alzheimer's disease. J Neurochem. 2024;168:3574–98.
59. Ammar RA, Mohamed AF, Kamal MM, Safar MM, Abdelkader NF. Neuroprotective effect of liraglutide in an experimental mouse model of multiple sclerosis: role of AMPK/SIRT1 signaling and NLRP3 inflammasome. Inflammopharmacology. 2022;30:919–34.
60. den Brok MH, Raaijmakers TK, Collado-Camps E, Adema GJ. Lipid Droplets as Immune Modulators in Myeloid Cells. Trends Immunol. 2018;39:380–92.

Figures

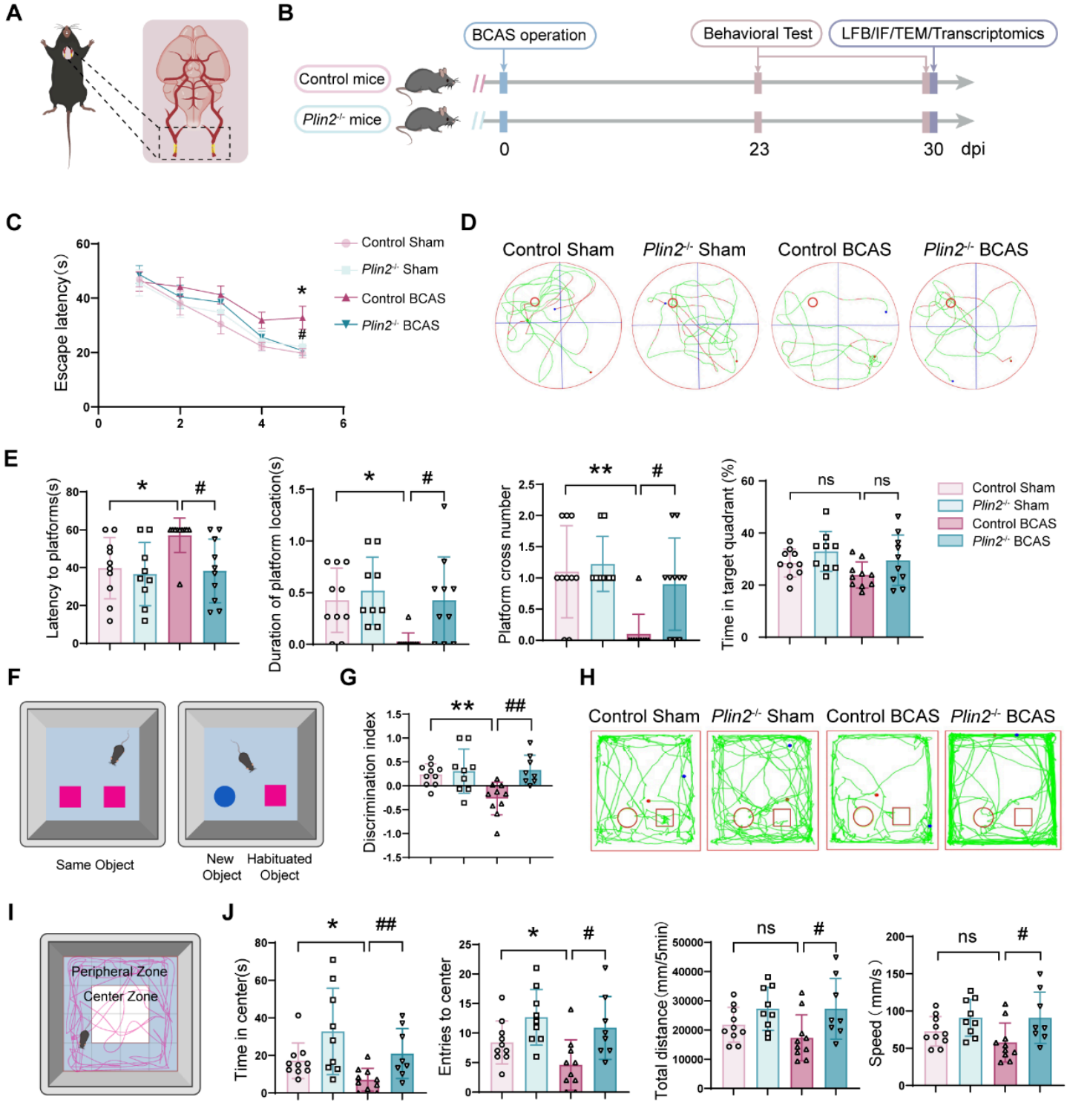


Figure 1

Microglial*Plin2* knockout alleviates cognitive impairment and anxiety-like behavior in BCAS mice.

(A), Surgical diagram of BCAS induction. (B), Experimental timeline. (C), Morris water maze (MWM) escape latency. *P<0.05 Vs Control Sham; #P<0.05 Vs Control BCAS. (D), Representative MWM movement trails. (E), Platform-related parameters in MWM. *P<0.05, **P<0.01 Vs Control Sham; #P<0.05

Vs Control BCAS. (F), Novel object recognition (NOR) test schematic. (G), NOR discrimination index. **P<0.01 Vs Control Sham; ##P<0.01 Vs Control BCAS. (H), Representative NOR movement trails. (I), Open field test (OFT) schematic. (J), OFT behavioral parameters. *P<0.05 Vs Control Sham; #P<0.05, ##P<0.01 Vs Control BCAS. Data are analyzed by one-way ANOVA with Tukey's test; n=9-10 per group.

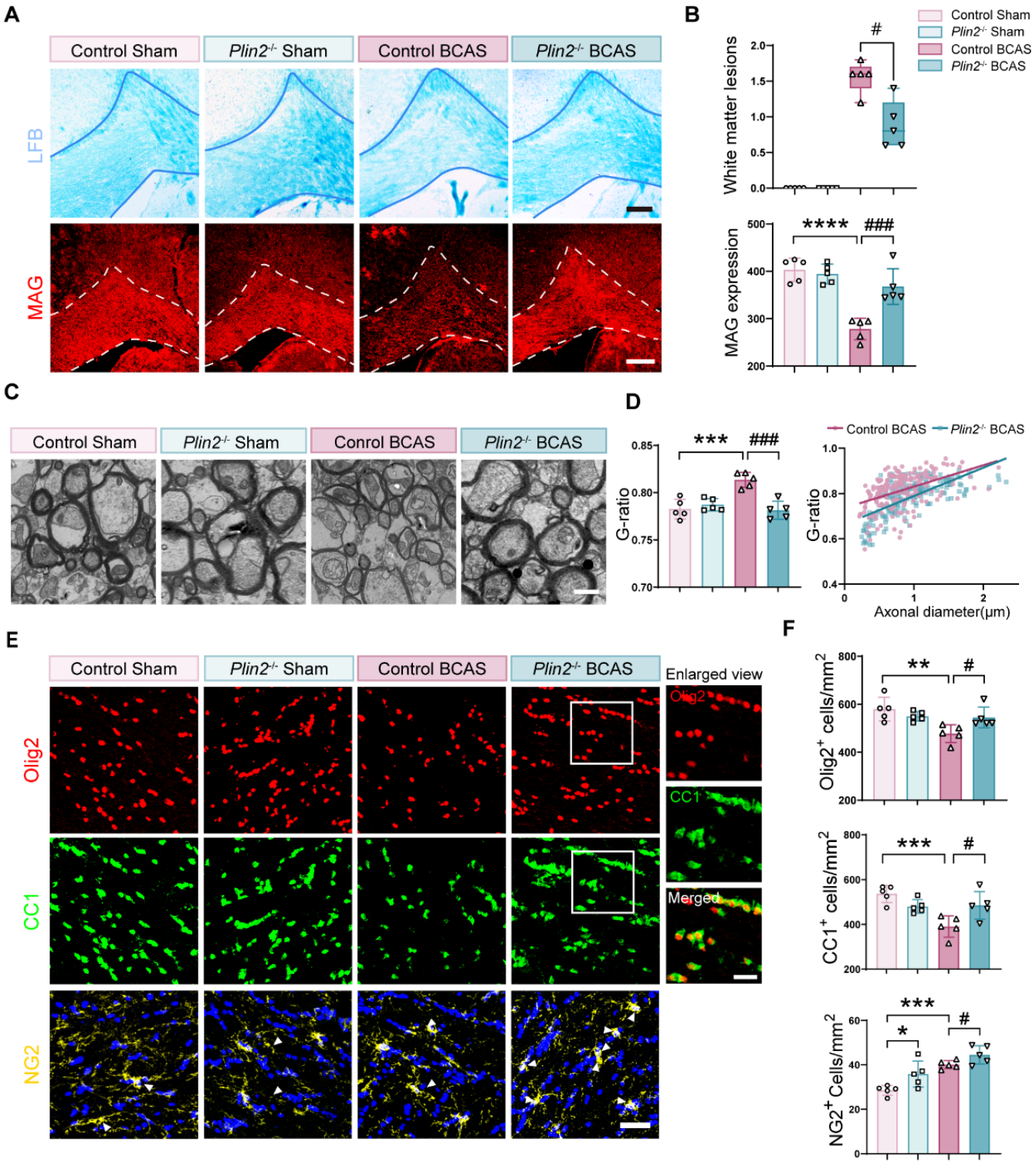


Figure 2

Microglial *Plin2* deficiency attenuates white matter injury and promotes remyelination after BCAS.

(A), Representative LFB staining and MAG immunofluorescence in corpus callosum. Scale bar: 150 μm. (B), Quantification of LFB scores and MAG expression. #P<0.05 Vs Control BCAS; ****P<0.0001 Vs Control Sham; ###P<0.001 Vs Control BCAS. (C), Representative electron micrographs of myelinated axons. Scale bar: 1 μm. (D), G-ratio quantification. ***P<0.001 Vs Control Sham; ###P<0.001 Vs Control BCAS. (E), Immunofluorescence for CC1, Olig2 and NG2. Scale bars: 40 μm (15 μm enlarged views). (F), Quantification of $CC1^+$, $Olig2^+$ and $NG2^+$ cells. *P<0.05, **P<0.01, ***P<0.001 Vs Control Sham; #P<0.05 Vs Control BCAS. Data: Mean ± SEM; n=5 mice/group. LFB score: Mann-Whitney U test; others: one-way ANOVA with Tukey's test. G-ratio analysis: 200 axons/group.

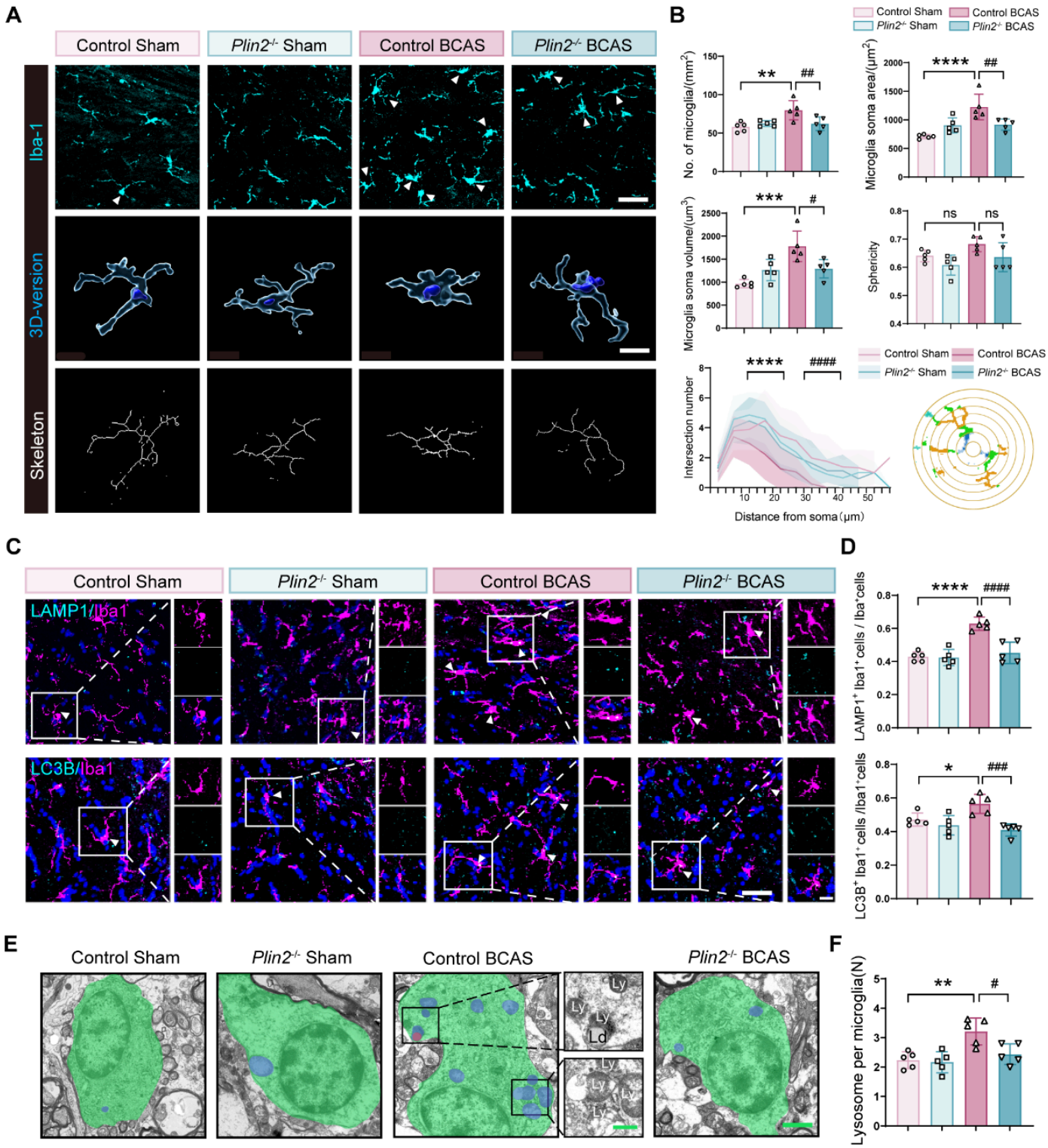


Figure 3

***Plin2*deletion alleviates microglial activation and restores the autophagy-lysosomal pathway in BCAS mice.**

(A), Representative immunofluorescence, 3D-reconstructed, and skeletonized images of microglia. Scale bars: 60 μm (immunofluorescence), 10 μm (3D and skeletonization). (B), Quantification of microglial

number, soma area/volume, sphericity, and Sholl intersection number. Sholl mask shown (right). **P<0.01, ***P<0.001, ****P<0.0001 Vs Control Sham; #P<0.05, ##P<0.01, ####P<0.0001 Vs Control BCAS; ns, no significance. (C), Confocal images of LAMP1 and LC3B colocalization with Iba1. Scale bars: 40 μm, 10 μm (enlarged view). Arrowheads indicate double-labeled cells. (D), Quantification of LAMP1 and LC3B colocalization with microglia. *P<0.05, ****P<0.0001 Vs Control Sham; ###P<0.001, ####P<0.0001 Vs Control BCAS; ns, no significance. (E), Electron microscopic images of microglia. Scale bars: 2 μm, 0.5 μm (enlarged view); Ly, lysosome; LD, lipid droplet. (F), Quantification of lysosome number in microglia. **P<0.01 Vs Control Sham; #P<0.05 Vs Control BCAS. Data: Mean ± SEM; n=5 mice/group. One-way ANOVA with Tukey's test.

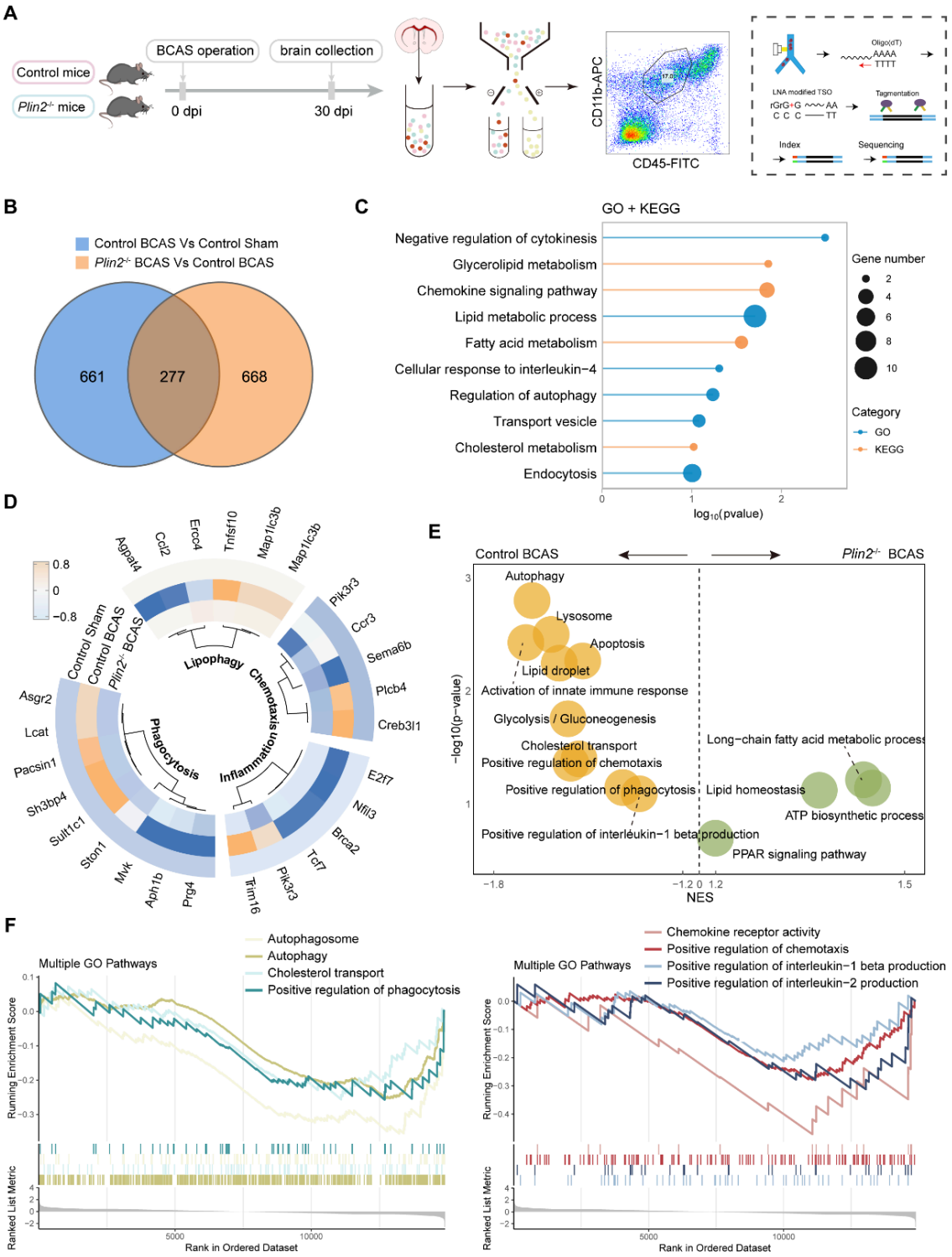


Figure 4

Plin2 deficiency reprograms microglial metabolic and inflammatory pathways after BCAS.

(A), Schematic of microglia sorting by flow cytometry and Smart-seq library construction. (B), Venn diagrams of significantly differentially expressed genes (DEGs) and overlapping DEGs between comparison groups. (C), GO and KEGG pathway enrichment analysis of common DEGs. (D), Circular

heatmap showing expression patterns of genes related to Lipophagy, Phagocytosis, Inflammation, and Chromatin analysis. (E), Gene Set Enrichment Analysis (GSEA) and representative enrichment plots for autophagy, lipid metabolism, and immune response pathways. (F), Representative GSEA enrichment plots for key biological processes.

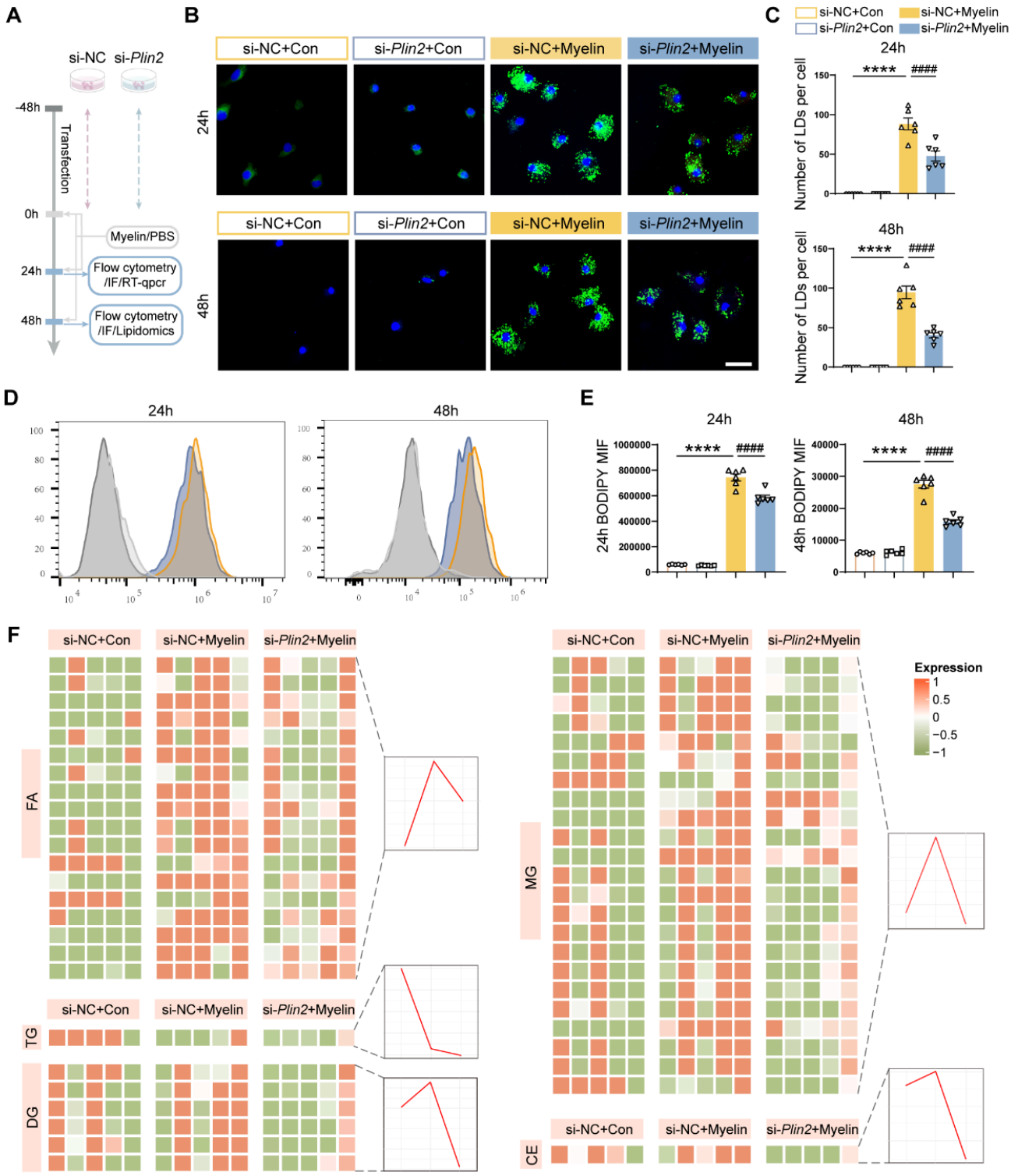


Figure 5

***Plin2*deficiency reduces lipid droplet accumulation and reprograms lipid metabolism in myelin debris–engulfing microglia.**

(A), Experimental design for lipid droplet (LD) analysis and lipidomics in primary microglia. (B), Representative confocal images of BODIPY staining in microglia. Scale bar: 30 μm. (C), Quantification of LD number per cell. ****P<0.0001 Vs si-NC+Con; ####P<0.0001 Vs si-NC+Myelin. (D), Representative flow cytometry histogram of BODIPY fluorescence. (E), Quantification of BODIPY mean fluorescence intensity. ****P<0.0001 Vs si-NC+Con; ####P<0.0001 Vs si-NC+Myelin. (F), Heatmap showing lipid profiles across groups, highlighting differentially expressed fatty acids, triglycerides, diglycerides, monoglycerides, and cholesterol esters. Data: Mean ± SEM; n=5-6 per group. One-way ANOVA with Tukey's test.

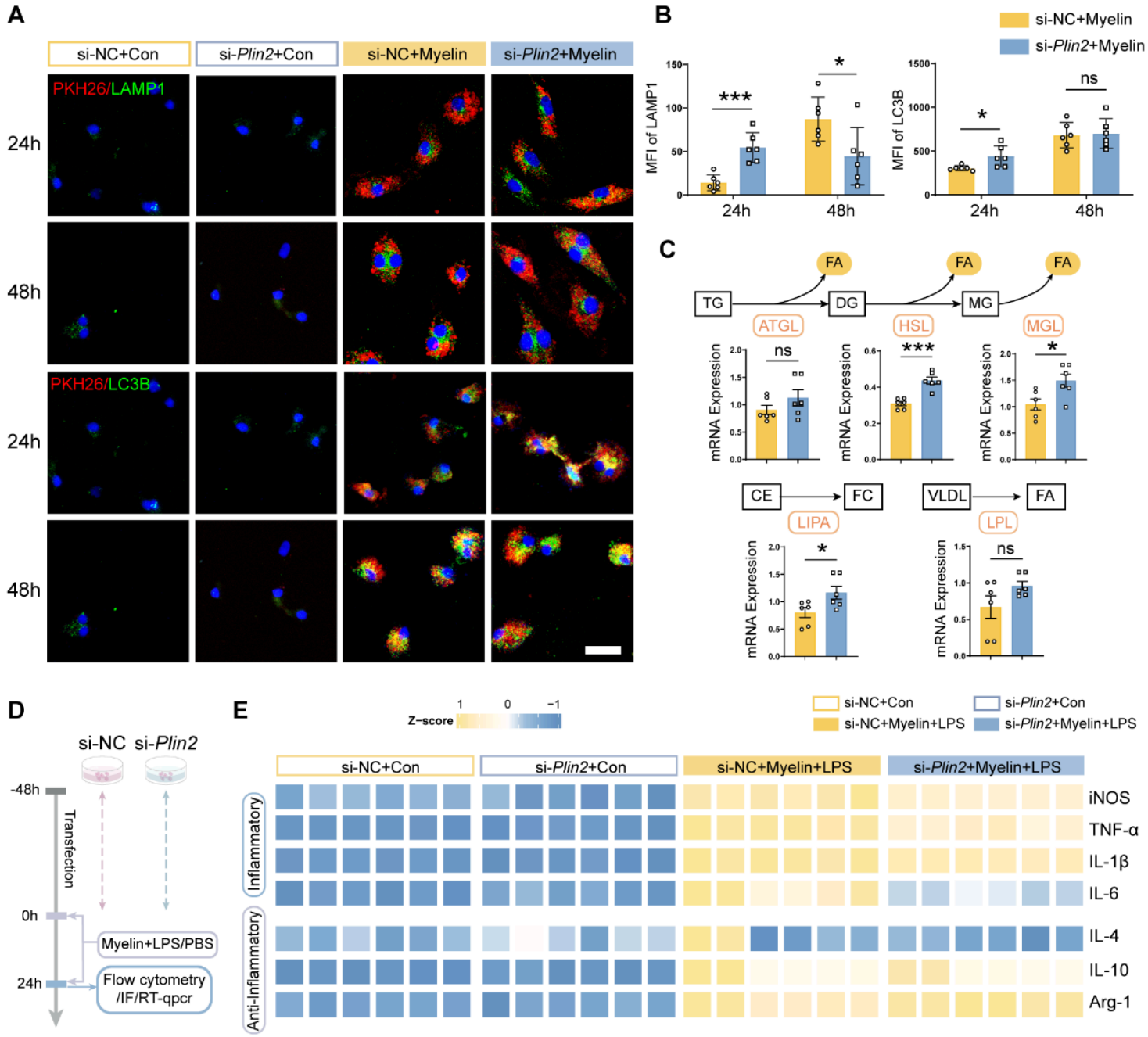


Figure 6

***Plin2*deficiency attenuates microglial inflammation by promoting lipid droplet catabolism via coordinated lipophagy and lipolysis.**

(A), Confocal images of LAMP1, LC3B, and Iba1 co-staining in primary microglia at 24 h and 48 h. Scale bar: 30 μm. (B), Quantification of LAMP1 and LC3B mean fluorescence intensity in Iba1⁺ cells. *P<0.05, ***P<0.001 Vs si-NC+Myelin group (C), Normalized mRNA levels of triglyceride and cholesterol metabolism genes. *P<0.05, ***P<0.001 Vs si-NC+Myelin group. (D), Heatmap of normalized mRNA

levels for pro- and anti-inflammatory cytokines across groups. Data: Mean ± SEM; n=6 per group. One-way ANOVA with Tukey's test.

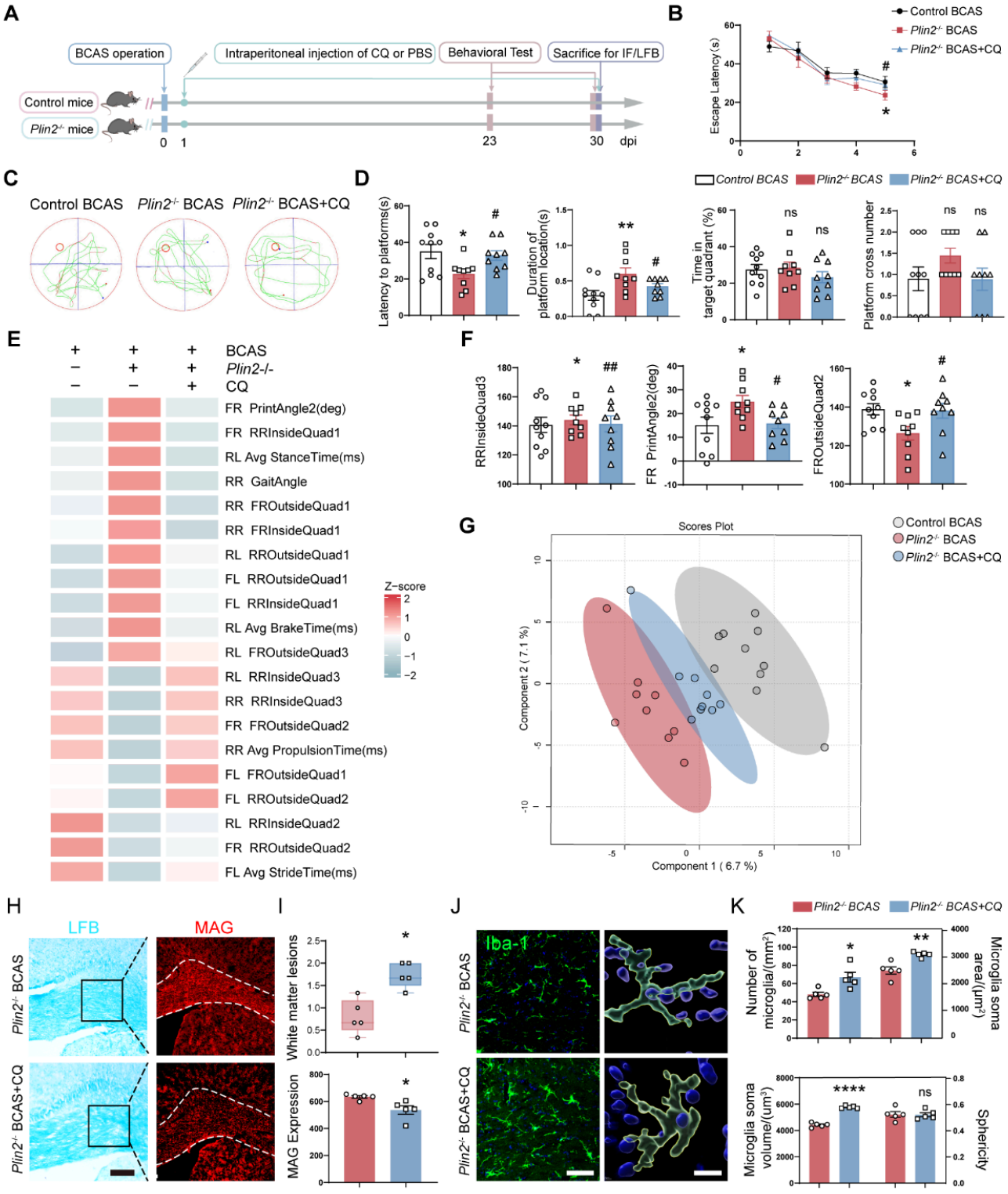


Figure 7

Inhibition of autophagy reverses the neuroprotective effects of *Plin2* deficiency in BCAS mice.

(A), Experimental timeline of BCAS, chloroquine (CQ) administration, behavioral tests, and tissue harvest. (B), Morris water maze escape latency. *P<0.05 Vs Control BCAS mice; #P<0.05 Vs *Plin2*$^{-/-}$ BCAS mice; ns, no significance. (C), Representative MWM movement trails. (D), MWM platform-related parameters and quadrant time. *P<0.05, **P<0.01 Vs Control BCAS mice; #P<0.05 Vs *Plin2*$^{-/-}$ BCAS mice; ns, no significance. (E), Heatmap of significantly different gait parameters from TreadScan analysis. (F), Specific TreadScan gait parameters (RRInsideQuad3, RRInsideQuad1, FROutsideQuad2). *P<0.05 Vs Control BCAS mice; #P<0.05 ##P<0.01 Vs *Plin2*$^{-/-}$ BCAS mice. (G), Partial least squares discriminant analysis of motor-associated indexes from TreadScan. (H), Representative LFB staining of corpus callosum. Representative confocal images of MAG of corpus callosum. Scale bars: 200 μm (I), Quantification of LFB scores. Quantitative analysis of the relative expression of MAG. *P<0.05 Vs *Plin2*$^{-/-}$ BCAS mice. (J), Representative immunofluorescence and 3D-reconstructed images of microglia. Scale bars: 60 μm, 10 μm. (K), Quantification of microglial number, soma area/volume, and sphericity. *P<0.05, **P<0.01, ****P<0.0001 Vs *Plin2*$^{-/-}$ BCAS mice; ns, no significance.
Data: Mean ± SEM; behavioral tests: n=9-10 mice/group, LFB/IF: n=5 mice/group.
MWM/TreadScan/microglia: one-way ANOVA with Tukey's test; LFB score: Mann-Whitney U test.

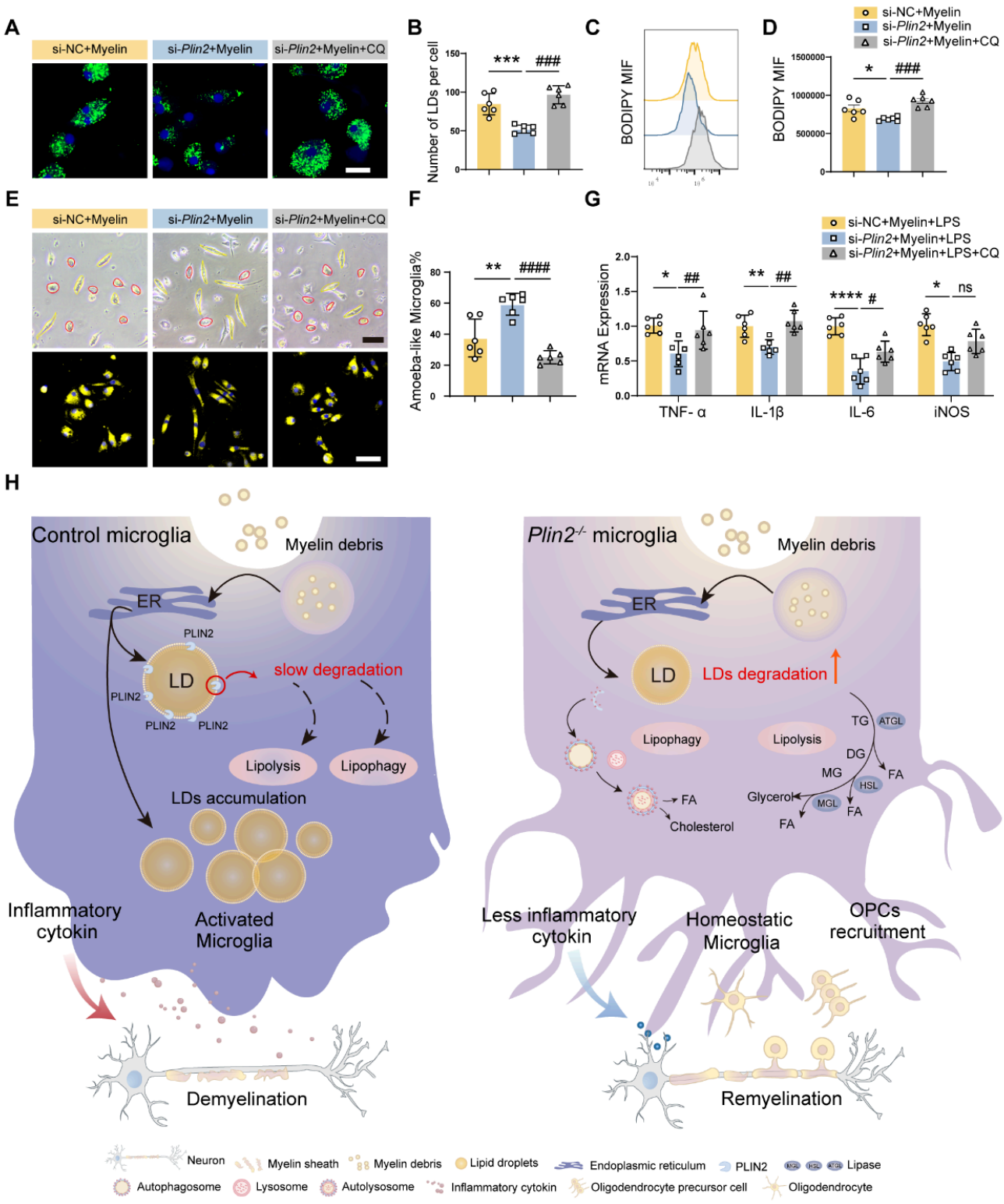


Figure 8

Inhibition of autophagy abrogates *Plin2* knockdown-mediated lipid clearance and restores microglial activation.

(A), Confocal images of BODIPY staining in microglia. Scale bar: 30 μm. (B), Quantification of lipid droplets (LDs) per cell. ****P<0.0001 Vs si-NC+Myelin+LPS; ####P<0.0001 Vs si-*Plin2*+Myelin+LPS. (C),

Representative flow cytometry histogram of BODIPY fluorescence. (D), Quantification of BODIPY mean fluorescence intensity. ****P<0.0001 Vs si-NC+Myelin+LPS; ####P<0.0001 Vs si-*Plin2*+Myelin+LPS. (E), Representative bright-field and Iba1 immunofluorescence images of cultured microglia. Scale bars: 60 μm, 40 μm. (F), Quantification of amoeboid microglia percentage. **P<0.01 Vs si-NC+Myelin+LPS; ####P<0.0001 Vs si-*Plin2*+Myelin+LPS. (G), Normalized mRNA levels of IL-6, IL-1β, TNF-α, and iNOS in cultured microglia under different treatments were evaluated by quantitative real-time polymerase chain reaction. (H), Graphic Abstract. Data: Mean ± SEM; n=6 per group. One-way ANOVA with Tukey's test.

Supplementary Files

This is a list of supplementary files associated with this preprint. Click to download.

- SupplementatyMaterials.docx